### Title
Seismic Imaging of the Mw 7.1 Ridgecrest Earthquake Rupture Zone From Data Recorded by Dense Linear Arrays




### Journal
Journal of Geophysical Research: Solid Earth, 126(7)

### ISSN
2169-9313



### Authors
Qiu, Hongrui
Ben-Zion, Yehuda
Catchings, Rufus
et al.



### Publication Date
2021-07-01

### DOI
10.1029/2021jb022043

Peer reviewed

# Seismic imaging of the Mw 7.1 Ridgecrest earthquake rupture zone from data recorded by dense linear arrays

Hongrui Qiu[1], Yehuda Ben-Zion[2,3], Rufus Catchings[4], Mark R. Goldman[4], Amir A. Allam[5], and Jamison Steidl[4,6]

[1]Department of Earth, Environmental and Planetary Sciences, Rice University, Houston, TX, USA

[2]Department of Earth Sciences, University of Southern California, Los Angeles, CA, USA

[3]Southern California Earthquake Center, University of Southern California, Los Angeles, CA, USA

[4]U.S. Geological Survey, 345 Middlefield Road MS 977, Menlo Park, California 94025-3591 U.S.A

[5]Department of Geology and Geophysics, University of Utah, Salt Lake City, UT, USA

[6]Earth Research Institute, University of California, Santa Barbara, CA, USA

Corresponding author: Hongrui Qiu (hongruiq@rice.edu, qiuhonrui@gmail.com)

**Key points**:

- Several 1- to 2-km-wide low-velocity zones with more intensely damaged inner cores (0.5-1.5 km wide) are identified beneath each array
- An automated detector, based on peak ground velocities and durations of high amplitude *S* waves, identifies fault-zone trapped waves
- The *P* wave delay time and *S* wave amplification patterns indicate consistent locations and widths of fault damage zones

## Abstract

We analyze seismograms recorded by four arrays (B1-B4) with 100-m station spacing and apertures of 4-8 km that cross the surface rupture of the 2019 Mw 7.1 Ridgecrest earthquake. The arrays extend from B1 in the northwest to B4 in the southeast of the surface rupture. Delay times between *P*-wave arrivals associated with ∼1200 local earthquakes and four teleseismic events are used to estimate local velocity variations beneath the arrays. Both teleseismic and local *P* waves travel faster on the northeast than the southwest side of the fault beneath arrays B1 and B4, but the velocity contrast is less reliably resolved at arrays B2 and B3. We identify several 1- to 2-km-wide low-velocity zones with much slower inner cores that amplify *S* waveforms, inferred as damage zones, beneath each array. The damage zones at arrays B2 and B4 also generate fault-zone head and trapped waves. An automated detector, based on peak ground velocities and durations of high-amplitude waves, identifies candidate fault-zone trapped waves (FZTWs) in a localized zone for ~600 earthquakes at array B4. Synthetic waveform modeling of averaged FZTWs, generated by ~30 events with high-quality signals, indicates that the trapping structure at array B4 has a width of ∼300 m, depth of 3-5 km, *S*-wave velocity reduction of ∼20% with respect to the surrounding rock, *Q*-value of ∼30, and *S*-wave velocity contrast of ~4% across the fault (faster on the northeast side). The results show complex fault-zone internal structures (velocity contrasts and low-velocity zones) that vary along fault strike.

## Plain Language Summary

The 2019 Mw 7.1 Ridgecrest earthquake in the Eastern California Shear Zone generated a vigorous aftershock sequence that provided a wealth of seismic data. We derive subsurface structural properties within and across the Ridgecrest rupture zone from seismic waveforms generated by the earthquake sequence. The data are recorded by four dense nodal arrays that were deployed across the Ridgecrest rupture zone with ~100 m spacing and aperture of a few kilometers. Delay times of *P* wave and amplification of *S* waves are used to infer on several 1-2-km-wide low-velocity zones with more intensely damaged inner cores (0.5-1.5 km wide) beneath each array. Waveform modeling of fault

zone trapped waves well-recorded by one array provides geometrical and seismic properties of a coherent waveguide in the damage fault zone structure at that location. The results are complementary to tomographic models that provide a regional context but do not resolve internal structural elements of the Ridgecrest rupture zone.

## 1. Introduction

The Mw 7.1 Ridgecrest earthquake of July 5, 2019 and the earlier Mw 6.4 event on July 4 in the southern part of the Walker Lane shear zone (Fig. 1) were felt throughout southern California and produced a vigorous aftershock sequence. These events led to rapid deployments of seismic arrays across and around the Ridgecrest earthquake sequence (Catchings et al., 2020). Kinematic rupture processes of the Mw 6.4 and Mw 7.1 events, surface deformation, and properties of the aftershocks show complex patterns, with strong variations both along strike of the rupture zones and in depth (e.g., Chen et al., 2020; Cheng & Ben-Zion, 2020; Jia et al., 2020; Ross et al., 2019; Xu et al., 2020). Data recorded by several dense arrays crossing the rupture zone of the Mw 7.1 earthquake can be used to derive high-resolution seismic information on the internal structure of the rupture zone. Detailed imaging of the structure associated with the rupture zone can provide important information on various topics, including initiation and arrest of ruptures (e.g., Aki, 1979; King, 1986), amplification of seismic waves (e.g., Kurzon et al., 2014; Rovelli et al. 2002; Spudich & Olsen, 2001), interactions of ruptures with fault zone properties (e.g., Ben-Zion & Huang 2002; Brietzke & Ben-Zion 2006; Huang et al., 2014), and properties of earthquake sequences (e.g., Thakur et al., 2020).

Several velocity models for the Ridgecrest area provide information for volumes with spatial resolutions ranging from several km (e.g., Lee et al., 2014; Shaw et al., 2015) to about 500 m (White et al. 2020). Structures in the top 1-2 km are poorly resolved in these velocity models due to limitations of the input data. Analyses of seismic data recorded by arrays across faults and rupture zones have proven highly effective in complementing regional velocity models and imaging sharp bimaterial interfaces and damage zones with width of a few tens of meters (e.g., Ben-Zion et al., 2003; Cochran et al., 2009; Li et al., 1994; Peng et al., 2003; Qin et al., 2018; Qiu et al., 2017; Share et al., 2019).

In this study, we investigate the seismic and geometrical properties of the damage structure associated with the 2019 Mw 7.1 Ridgecrest earthquake, based on the data obtained from four dense linear seismic arrays (B1-B4; triangles in Figs. 1 and 2) located across segments of the rupture. Analyses of the arrival patterns of *P* waves from both teleseismic and local seismic events across each array helps to detect and constrain properties of velocity contrasts across fault sections and low-velocity zones reflecting at least partially damaged rock. We identified fault-zone trapped waves, i.e., amplified motions of *S* waves associated with core damage zones that are sufficiently coherent to act as a waveguide, at some locations and inverted for average geometrical and seismic properties of the fault-zone waveguide.

In the following sections, we describe the deployment and data processing in section 2 and present the methodology and results on various aspects of the fault-zone structures from different types of observations in section 3. The imaging results from different phases and analyses are summarized and discussed in section 4. The results show overall complex fault-zone structures that vary along the rupture strike, in general agreement with fault surface traces (Xu et al., 2020), seismic catalog (Ross et al., 2019) and potency of aftershocks (Cheng & Ben-Zion, 2020) in the Ridgecrest area.

## 2. Data & basic processing

Four linear arrays, with about 100-m station spacing and apertures of 4-8 km, were deployed across the surface rupture of the 2019 Mw 7.1 Ridgecrest earthquake (Fig. 1). The arrays extended from B1 in the northwest to B4 in the southeast of the surface rupture (Fig. 2). In total, the B-arrays consisted of 248 Fairfield and SmartSolo sensors that recorded continuously at 500 Hz for about a one-month period (7/12/2019-8/8/2019).

For teleseismic delay time analysis (Section 3.1), we use the Taup toolkit (Crotwell et al., 1999) and velocity model IASP91 (Kennett & Engdahl, 1991) for predictions of *P*-arrival time at each station. The teleseismic earthquakes have epicentral distances between 30-90°, depth > 50 km, and Mw > 6.0. For analysis of local *P* waves (Section 3.2), we first extract the seismic waveforms generated by ~1200 local events (red box in Fig. 1) at each station and use the catalog of Hauksson et al. (2012, extended to 2019) for locations. The mean and linear trend are removed from the waveforms, and a bandpass filter between 0.5 Hz and 20 Hz is applied. In the study of fault zone trapped waves (Section 3.3), the north-south and east-west components are rotated to a coordinate system parallel and perpendicular to the fault strike.

## 3. Analysis

We conduct three types of studies involving different signals and spatial scales to image several components of the fault-zone structure associated with the 2019 Mw 7.1 Ridgecrest earthquake beneath the four linear arrays (Fig. 2). We describe the analyses below, starting with large-scale structural features (e.g., overall velocity variations across the fault) and progressing to inner fault-zone components (e.g., geometry and velocity of the damage zone). The results are obtained using teleseismic delay-time analyses (DTA), local *P*-wave DTA, and analysis associated with FZTWs following the *S*-wave arrival.

### 3.1 Teleseismic delay time analysis

During the one-month deployment, teleseismic *P* waves with sufficient signal to noise ratios (SNR > 5) between 0.5 Hz and 2 Hz were recorded for three events at array B1 and four earthquakes at arrays B2-B4 (Figs. S1- S4). We do not investigate teleseismic *S* waves since they have SNR < 5.

#### *3.1.1 Methodology*

As shown in previous studies (e.g., Ozakin et al., 2012; Qiu et al., 2017), there are three contributing factors to travel-time delays observed on a linear array for a teleseismic arrival: the geometry between the incoming plane wave and the array, topography, and the crustal structure beneath the array. To obtain the travel-time delays due to local crustal structures, we first predict the arrival time of the teleseismic *P*-wave for each station and event pair using the IASP91 model and assume the station is at sea level. Then, teleseismic *P* waveforms are bandpass filtered between 0.5 Hz and 2 Hz. By aligning the teleseismic *P* waves with respect to the corresponding predicted arrival time (Fig. 3b) at each station, we remove the delay times associated with the non-vertical incidence angle of incoming waves. This assumes a flat Moho interface beneath the array, which is likely given the small area involved and receiver function results (e.g., Zhu & Kanamori, 2000).

In Qiu et al. (2017), the *P* waveform is first stacked over the entire array for a specific teleseismic event and used as the reference. Then, the arrival-time pattern of *P* waves is extracted from cross-correlations of the *P* waveform recorded at each station and the reference waveform. However, this method is accurate only for arrays with short aperture (e.g., ~500 m in Qiu et al., 2017) when *P*-wave delay times are small (e.g., ~0.01 s). For arrays with long aperture, the *P* waveform recorded at a specific station may be used as the reference. Considering the long aperture of the B-arrays (4-8 km; Fig. 2), we estimate the *P*-wave delay time pattern by cross-correlating waveforms within a narrow *P*-wave window (Fig. 3b) for every pair of stations *i* and *j*. The center of the narrow *P*-wave window is determined based on the array-mean envelope function (Fig. 3b), and the peak frequency of the array-mean *P*-wave amplitude spectrum (Fig. 3c) is used to set the window width to be twice the dominant period. To further enhance the *P*-wave signals, we apply another filter with a narrower frequency band (black dashed lines in Fig. 3c) to the teleseismic data prior to the cross-correlation.

Let $\tilde{t}_{ij}$ be the time delay corresponding to where the cross-correlation function between *P* waveforms recorded at the *i*- and *j*-th stations reaches the maximum,

$$\tilde{t}_{ij} = \tilde{T}_i - \tilde{T}_j, \tag{1a}$$

where $\tilde{T}_i$ and $\tilde{T}_j$ are the teleseismic *P*-wave travel times at the *i*- and *j*-th stations, respectively. Since the mean of the arrival time pattern $\tilde{T}_i$ has no significance for our imaging, we can ignore the constant $\tilde{T}_j$ in equation (1a) and the delay time pattern is given by $\tilde{T}_{i\_j} = \tilde{t}_{ij}$ when the *j*-th station is fixed and set to be the reference. We note that the delay time patterns obtained by using different reference stations should be consistent, i.e., $\tilde{T}_{i\_j_1} - \tilde{T}_{i\_j_2}$ is a constant. Thus, we can minimize the measurement error by averaging equation (1a) over *j*,

$$\tilde{T}_i = \sum_{j=1}^{N} \tilde{t}_{ij} \Big/ N + \sum_{j=1}^{N} \tilde{T}_j \Big/ N = \sum_{j=1}^{N} \tilde{t}_{ij} \Big/ N + C, \tag{1b}$$

where $N$ is the number of stations and $C$ is a constant. We again ignore the constant $C$ and remove the effect of un-modeled topography from the teleseismic $P$-wave delay time

$$T_i = \sum_{j=1}^{N} \tilde{t}_{ij} \Big/ N - \Delta h_i / v_{\mathrm{corr}}, \tag{2}$$

where $v_{\mathrm{corr}}$ is the $P$-wave velocity (Vp) and $\Delta h_i = h_i - \sum_{j=1}^{N} h_j / N$ represents the relative topography, with $h_i$ indicating the elevation at the $i$-th station (Figs. 2b-e). Here, for the topographic correction, we assume a vertical-incidence angle for the incoming $P$ wave and a constant Vp that is likely representative of velocity structures averaged over the top 1-2 km (e.g., Park et al., 2019). Since the velocity structure at the shallow section is poorly constrained by existing velocity models, we use two constant Vp values, 2 km/s and 4 km/s, to estimate the lower and upper limits of $v_{\mathrm{corr}}$.

*3.1.2 Results*

Coherent *P* arrivals, with different peak frequencies, are observed crossing the array for the four events in Figure S1. Although the frequency content of the *P* waveforms is different between events, the obtained arrival patterns prior to topographic correction are in general consistent (e.g., higher velocity in the northeast beneath array B4 in Fig. 4d). The black curves in Figure 4 depict the teleseismic *P*-arrival patterns for each array averaged over all events with the standard deviation of the mean giving the uncertainty, and the delay times after correcting the array topography are illustrated as colored dashed curves. Features of delay-time patterns associated with a velocity contrast across the fault (i.e., a smoothed step function as in Fig. 6d of Qiu et al., 2017) and a low-velocity zone (i.e., a mountain-shaped function as in Fig. 6b of Qiu et al., 2017) are both observed in the results after the topographic correction.

Delay-time patterns resolved at arrays B1 and B4 yield clear velocity contrasts across the fault, with the southwest block having later arrivals indicating slower velocity (~0.15 s and ~0.25 s in *P*-wave arrival time; Figs. 4a and 4d). Topographic corrections have minor effects on the resolved arrival-time patterns at both arrays, as differences between the two dashed curves are negligible in Figures 4a and 4d. Compared to the pattern dominated by the velocity contrast, the time delay associated with low-velocity zones is less obvious and comparable to the level of uncertainties (Figs. 4a and 4d). In contrast, the dominant feature in arrival patterns resolved at arrays B2 and B3 yields several ~1-km-wide low-velocity zones that generate a maximum time delay of ~0.04 s (Figs. 4b-c): two centered at about 2.5 km southwest and 0.5 km northeast of the center of array B2; one centered at ~0.5 km southwest of the B3 array center.

Although the topographic correction has negligible effects on the low-velocity zones resolved at arrays B2 and B3, the time delays associated with velocity contrasts across the fault beneath the two arrays are much weaker and vary significantly with the Vp used in the correction (Figs. 4b-c). Different from the other three arrays, the polarity of the velocity contrast at array B3 is flipped for arrival patterns resolved using Vp of 2 km/s and 4 km/s. This is likely due to the combination of the larger difference in topography and smaller velocity contrast at arrays B2 and B3. Therefore, we do not discuss the velocity contrasts resolved from teleseismic *P* waves recorded at arrays B2 and B3 in later sections.

## 3.2 Local *P*-wave delay time analysis

*P* waves from local earthquakes recorded by the B-arrays are observed at higher frequencies (peaks at ~8 Hz; e.g., Fig. 5a) compared to those of teleseismic events (between 0.5-2 Hz; e.g., Fig. 3). Thus, higher resolution images of local fault zone structures can be achieved by analyzing arrival times of direct *P* waves from local earthquakes across each array.

### *3.2.1 Methodology*

Compared with teleseismic arrivals, the effect of source-receiver geometry on *P* waves for local earthquakes recorded by an array requires additional processing than the plane wave correction used in section 3.1.1. To extract the variations in *P*-wave arrival times associated with local fault-zone structures, we first suppress the contributions from source-receiver geometry and topographic variations by dividing the time axis of the *P* waveform recorded at the *i*-th station for event *j* with its corresponding propagation distance $H_{ij}$ (e.g., from Fig. 5a to 5b). Here, we use the hypocentral distance to approximate $H_{ij}$. *P*-wave picks, $s_{ij} = t_{ij}/H_{ij}$ in units of slowness (e.g., Figs. 5b and S5b-S7b), are then picked via the short-term-average/long-term-average (STA/LTA) algorithm (Allen, 1978) using waveforms within the slowness range of 0.15-0.25 s/km (to exclude the effect of *S* waves). The *P*-wave SNR is calculated as the ratio between the maximum and root mean square amplitudes of waveforms in slowness windows from $s_{ij}$ to 0.25 s/km and 0.15 s/km to $s_{ij}$, respectively. *P*-wave picks with SNR less than 10 are not used, and events are excluded if less than 80% of the array shows good quality *P*-wave picks (SNR > 10).

The array-mean slowness $\bar{s}_j = \sum_{i=1}^{M} s_{ij}/M$, with *M* being the number of stations, can vary significantly with focal depth and epicenter location (due to 3-D velocity structures). Therefore, we use relative slowness, $\hat{s}_{ij} = s_{ij}/\bar{s}_j$ (e.g., Qiu et al., 2017; Share et al., 2017) to characterize statistical features of the local structure-related *P*-wave arrival pattern using all available events. We can also estimate the local structure-related *P*-wave arrival pattern in delay time, $\delta t_{ij}$ for station *i* and event *j*, as $\delta t_{ij} = \left(s_{ij} - \bar{s}_j\right) \cdot H_{ij}$. Since the existing velocity models indicate that structures in the Ridgecrest area are highly heterogeneous, we only analyze *P* waves from events with depth > 5 km and close to each array (red box in Figs. 5c and S5c-S7c) to ensure that the hypocentral distance is a good approximation of the propagation distance $H_{ij}$ and the resolved delay time pattern is representative of local structures beneath the array.

Based on previous fault zone studies (e.g., Qiu et al., 2017; Share et al., 2017), the observed *P*-wave travel time at station *i* for a near-fault event *j* mainly consists of two components:

$$t_{ij} = s_{ij} \cdot H_{ij} \approx \bar{s}_j \cdot H_{ij} \cdot (1 + \eta_i) + \Delta t_{ij}. \tag{3}$$

The first term of equation (3) indicates the time delay associated with the cross-fault velocity contrast beneath the array, and, ideally, $\eta_i$ is a step function, i.e., equals $-\eta/2$ and $\eta/2$ ($\eta < 1$) for stations on the faster and slower crustal blocks, respectively. The second term $\Delta t_{ij}$ represents the contribution of local structures beneath the array at shallow depth (e.g., fault damage zone, sedimentary basin). Let $\theta_j$ be the average incident angle of *P* waves from event *j* to the array, $\Delta t_{ij}$ is inversely proportional to $\cos\theta_j$, i.e., $\Delta t_{ij} \approx \tau_i/\cos\theta_j$, where $\tau_i$ is the delay time of a vertically incident *P* wave associated with shallow structures beneath the array at station *i*.

Following the derivation in Text S1, the arrival patterns averaged over all near-fault and close-to-array events are approximately given by:

$$\hat{S}_i = \sum_{j=1}^{N} \hat{s}_{ij} \Big/ N \approx 1 + \eta_i + \tau_i / \left(\tilde{t}_i \cos \tilde{\theta}\right) \approx 1 + \eta_i + \tau_i / \left(\tilde{t} \cos \tilde{\theta}\right), \tag{4a}$$

in relative slowness, and

$$\delta T_i = \sum_{j=1}^{N} \delta t_{ij} \Big/ N \approx \eta_i \cdot \bar{t}_i + \tau_i / \cos \tilde{\theta} \approx \eta_i \cdot \bar{t} + \tau_i / \cos \tilde{\theta}, \tag{4b}$$

in delay time, after dropping the higher order terms. $\tilde{t}_i$ and $\bar{t}_i$ are the harmonic and arithmetic means of *P*-wave travel time $t_{ij}$, respectively, over all events. *N* is the number of events and $\tilde{\theta}$ is the mean incidence angle averaged over all events. $\tilde{t}$ and $\bar{t}$ denote the array-mean travel times of $\tilde{t}_i$ and $\bar{t}_i$, respectively. It is interesting to note that the shape of arrival patterns $\hat{S}_i$ and $\delta T_i$ is the same, i.e., $\delta T_i / \left(\hat{S}_i - 1\right)$ is a constant, when $\tilde{t} \approx \bar{t}$.

*3.2.2 Results*

Figure 6a shows the results of statistical analysis on the local structure-related *P*-wave arrival pattern in relative slowness ($\hat{S}_i$ in eq. 4a) and delay time ($\delta T_i$ in eq. 4b) for array B1 using 189 near-fault events with depth > 5 km outlined by the red box in Figure 5c. The relative slowness patterns are averaged over all analyzed events and the standard deviation of the mean is used to estimate the uncertainty. The small error bars and confined width of histograms suggest that the mean relative slowness curve is representative of the patterns observed from all analyzed events. The mean pattern in delay time ($\delta T_i$) with small uncertainties (Fig. 6a) is observed to have the same shape as that of the relative slowness, i.e., $\delta T_i / \left(\hat{S}_i - 1\right)$ is approximately a constant. This is consistent with equation (4) when $\tilde{t} \approx \bar{t}$.

Good agreement between the mean patterns of relative slowness and delay time with small uncertainties is also observed at arrays B2-B4 in Figures 6c, 6e, and 6g. Consistent with the teleseismic *P*-wave arrival time pattern shown in Figure 4, we observe the features of delays in local *P*-wave arrival time associated with a step-function-like and several mountain-shaped components at each array (left panels of Fig. 6) that likely correspond to a velocity contrast across the fault and low-velocity zones, respectively.

Similar mean patterns of relative slowness are also observed for subsets of events grouped according to different narrow ranges of depth (Figs. S8a-S11a). The polarity of the velocity contrast is the same for arrays B1 and B4 (Figs. 6a and 6g), with the southwest block being slower, consistent with results of the teleseismic delay time analysis (Figs. 4a and 4d). However, delay time patterns at arrays B2 and B3 show the opposite polarity (Figs. 6c and 6e), i.e., the northeast block having slower velocity. This is consistent with results of the teleseismic delay time analysis before the topographic correction (Figs. 4b-c).

We note that delay times associated with shallow materials ($\tau_i$ in eq. 4a) could also yield a step-function-like pattern (e.g., variations in sediment thickness across fault). Thus, the amplitude of the step-function-like component, $\tilde{\eta}$, is an upper limit of the magnitude of the cross-fault velocity contrast. We measure the amplitude of $\tilde{\eta}$ as the difference between relative slowness values averaged over stations on the southwest and northeast edges of the array (left panels of Fig. 6), and the values are 5.3%, 0.8%, 3.9%, and 8.8% at the sites of arrays B1-B4, respectively. Following equation (4a), if the observed step-function-like pattern is due to variations in shallow materials, i.e., $\tau_i/\left(\tilde{t}\cos\tilde{\theta}\right)$, the amplitude of $\tilde{\eta}$ should decrease with depth as the mean incidence angle $\tilde{\theta}$ and travel time $\tilde{t}$ increase with propagation distance. This contradicts the observations that $\tilde{\eta}$ increases with depth at array B2 (Fig. S9a) and only slightly varies with depth at arrays B1 (Fig. S8a), B2 (Fig. S10a), and B4 (Fig. S11a), suggesting the observed step-function-like pattern is likely a good approximation of the cross-fault velocity contrast, if the contribution due to elevation variation is negligible.

To further analyze the effect of array topography in the step-function-like component $\tilde{\eta}$, we first model the delay times of cross-fault velocity contrast (i.e., $\eta_i \cdot \bar{t}$ in eq. 4b) with a smoothed step function (Text S2). The modeled delay times of cross-fault velocity contrast consist of three components: a linear trend within a transition zone between two groups of stations at the southwest and northeast edges with constant values (eq. S5 in Text S2; Fig. 6). We then illustrate the location of the resolved transition zone beneath each array in Figure 2. At array B2, the span of the transition zone covers the area with a steep slope in the array topography (Fig. 2c). Considering the large variation in elevation (> 100 m) and the small amplitude of $\tilde{\eta}$ (0.8%), we conclude that the modeled cross-fault velocity contrast may be dominated by the residual in topographic correction rather than structure-related delay times. In contrast, for the other three arrays, the topography variation is less significant and the amplitude of $\tilde{\eta}$ is much larger (> 4%), indicating the array topography likely has negligible contribution to the modeled cross-fault velocity contrast.

The width of these transition zones and their locations relative to fault surface traces provide additional information on the internal structures of the fault zone. At array B1, the southwest edge of the transition zone correlates well with the surface trace of the Mw 7.1 earthquake (Fig. 2b), which is indicative of asymmetric rock damage offset to the northeast (faster side). At array B3, the northeast edge of the transition zone agrees well with the surface trace of the Mw 6.4 earthquake. The data recorded by array B3, crossing the surface ruptures of both the Mw 6.4 and Mw 7.1 events, likely detect the velocity contrast across the fault that hosted the Mw 6.4 earthquake, with the northwest side being higher in velocity. An asymmetric rock damage offset to the faster side (northwest) is also observed beneath array B3 (Fig. 2d). At array B4, the transition zone is much wider and almost covers the entire array. This is consistent with the fact that the array is at the southeast end of the Mw 7.1 earthquake rupture, where the rupture zone has several surface traces and is less localized (Fig. 2e).

Low-velocity zones that further delay the *P*-wave arrivals are also observed at each array, in addition to the pattern associated with the cross-fault velocity contrast (left panels of Fig. 6). To highlight contributions from these low-velocity zones (i.e., $(\tau_i/\left(\tilde{t}\cos\tilde{\theta}\right)$ in eq. 4a), the right panels of Figure 6 show the mean delay time pattern by subtracting the modeled $\eta_i \cdot \bar{t}$ from $\delta T_i$ (eq. 4b). A heat map of delay times $\delta T_i$ after subtracting the modeled $\eta_i \cdot \bar{t}$ is also shown. Similar delay patterns of $\tau_i$ reflecting shallow materials beneath the array are seen using events within different narrow ranges of depth (Figs. S8b-S11b). The range of delay patterns related to the major low-velocity zones underneath each array are outlined with green dashed lines in Figure 6. The slower inner cores (with peak delay time > 0.03 s) of these low-velocity zones are marked by the red dashed lines.

Consistent with the teleseismic *P*-wave arrival patterns obtained at arrays B2 and B3 (Figs. 4b-c), we observe low-velocity zones with comparable widths centered at the same locations. In addition, we retrieve higher resolution images of the narrower and slower inner cores that correlate well with locations of the local peaks identified in the teleseismic *P*-wave delay time patterns (Figs. 4b-c). This is likely due to the shorter wavelength of local seismic *P* waves that can provide high-resolution images of internal fault-zone structures (e.g., Dahlen et al., 2000). Delay patterns related to low-velocity zones are also observed in the results for arrays B1 and B4 (Figs. 6b and 6h), which are hard to identify in the teleseismic delay time analyses (Figs. 4a and 4d) due to large uncertainties (i.e., insufficient number of analyzed events).

We note that consistent patterns of the cross-fault velocity contrast and low-velocity zones are observed (with different amplitudes) in results obtained using events with large along-fault distances (Figs. S8c-d, S9c-d, S10c-d, and S11c-d). To better visualize the locations of these major low-velocity zones with respect to the array configurations and fault surface traces, we depict the core and entire range of these zones in Figure 2. In general, locations of the identified low-velocity zones correlate well with surface traces of the 2019 Ridgecrest earthquake sequence (Fig. 2) inferred from Xu et al. (2020). This suggests that these low-velocity zones are likely indicative of fault damage zones or sedimentary basins around fault segments.

3.3 Fault-zone trapped waves

A low-velocity fault-damage zone that is sufficiently uniform over a given distance can act as a waveguide and generate, in addition to delay times and motion amplification, trapped waves resulting from constructive interference of critically reflected phases within the waveguide (e.g., Ben-Zion & Aki 1990; Igel et al., 1997; Jahnke et al., 2002). Such waves have been observed at many locations, including the San Jacinto fault zone (e.g., Lewis et al., 2005; Qin et al., 2018; Qiu et al., 2017; Share et al., 2019; Wang et al., 2019), the Parkfield section of the San Andreas fault (e.g., Li et al., 1990; Lewis and Ben-Zion, 2010; Ellsworth & Malin, 2011), and various other faults in California, Japan, Italy, Turkey, and other places. Catchings et al. (2016) used peak ground velocities of *P* and *S* waveforms recorded by cross-fault linear arrays to infer the location and width of the West Napa-Franklin fault zone. Similarly, we find fault-damage-zone-related amplification in data recorded by the B-arrays (e.g., Figs. 7 and S12) and use such amplification to detect FZTW candidates. In this section, we first infer the location and width of fault damage zones that produce FZTWs using waveforms for the fault-parallel component, and then use waveforms of these candidates recorded by array B4 to invert for properties (e.g., width, velocity, and attenuation) of the local fault-zone waveguide.

*3.3.1 Methodology*

Figure 7a shows *S* waveforms recorded on the fault-parallel component of array B4 for an example event (Fig. 1). Following Ben-Zion et al. (2003) and Qiu et al. (2017, Fig. S6), several preprocessing steps are applied to the data prior to FZTW analyses. These include instrument response removal, integration to displacement seismogram, tapering between 1 s before and 2 s after the *S* pick, and convolution with $1/t^{1/2}$ to convert a point-source response to that of an equivalent *SH* line dislocation source (e.g., Igel et al., 2002; Vidale et al., 1985). Compared to the raw recordings (Fig. S12), clearer Love-type waveform sections with large amplitudes and lower frequency are found at a group of stations (stations B416-423; Fig. 7a) in the southwest part of the array.

Figure 7b displays distributions of peak ground velocities (PGV) and root mean square amplitudes (RMS) of the fault-parallel-component *S* waveforms, normalized by the maximum value of the entire array. Large values of PGV and RMS are seen at stations with FZTW, with considerably higher amplitudes than at the rest of the array. We define the likelihood of a FZTW recorded by a station as the multiplication of PGV and RMS (Fig. 7b). The likelihood curve measured for each event is normalized by the maximum value of the entire array. After averaging the likelihood curves over all analyzed events, we highlight the array sections that have high likelihood of recording FZTWs (Fig. 8); these sections can be used to infer the location and width of fault-zone waveguides.

Since FZTWs are observed in *S* waveforms recorded at stations B416-B423 of array B4 for the example event in Figure 7a, we can also identify candidate events with similar good-quality FZTWs through template matching, i.e., cross-correlating the fault-parallel component *S* waveforms recorded by stations B416-B423 for each event with those of the example event. The trapped waves of candidate events (Fig. 9a) that yield cross-correlation coefficients higher than 0.85 (e.g., Fig. 9b) are averaged (Fig. 9c) and inverted for properties (e.g., width, shear velocities, and attenuation) of the average fault-zone waveguide using a genetic inversion algorithm (e.g., Ben-Zion et al., 2003; Lewis et al., 2005; Qiu et al., 2017).

We test a total of 10,000 models (50 generations and 200 models per generation) to obtain a good estimate of the fault-zone parameters in the inversion. Parameters of the best-fitting model and the 2,000 models (investigated in the last 10 generations) are extracted from the inversion. Because there are strong trade-offs between model parameters governing FZTWs (e.g., Ben-Zion, 1998; Jahnke et al., 2002; Peng et al. 2003), a successful inversion not only yields good waveform fits but also shows consistency between parameters of the best-fitting model and peaks of the probability density distributions of parameters developed in the last 10 generations. Additional details on the method can be found in section 3.4 of Qiu et al. (2017) and Ben-Zion et al. (2003).

### *3.3.2 Results*

Figure 8 shows the distributions of FZTW likelihood values as a function of station location, estimated at arrays B1-B4 for all events within the red box shown in Figure 1. The likelihood values averaged over all analyzed events are representative of the in-situ amplification in *S*-wave. A good correlation is found in locations between local maxima of the likelihood curve and slower inner cores of the low-velocity zones identified from the local *P*-wave delay time analysis (Section 3.2; Fig. 8). This suggests that the observed inner cores of these low-velocity zones not only significantly delay the *P* arrivals but also amplify the incoming *S* waves.

However, not all stations within the inner cores of low-velocity zones identified in Figure 6 yield the same peak value of FZTW likelihood (Fig. 8). At array B4, the location of the candidate fault-zone waveguide (B417-B422; Figs. 7a and 8d) is in good agreement with the inner core of low-velocity zones that yields the highest likelihood value. We do not detect candidate FZTW at stations within the other low-velocity zones with much lower peak likelihood values. This is consistent with detailed fault-zone studies at Parkfield (Lewis & Ben-Zion, 2010), the rupture zone of the 1992 Landers earthquake (Peng et al., 2003), and fault zones in Japan (Mamada et al. 2004; Mizuno et al. 2008). These studies showed that various sections of fault zones produce delay times and other signals of damaged rocks but are either too heterogeneous or have significant segmentation between sources and receivers to generate trapped waves (e.g., Igel et al. 1997, 2002; Jahnke et al. 2002).

Not all analyzed events show *S*-wave amplification patterns that are consistent with the averaged curve. We first detect candidate events that show high FZTW likelihood values at stations B417-B422 (Fig. 8d) by cross-correlating the likelihood pattern measured for each event (e.g., black curve in Fig. 7b) with that of the mean (e.g., red curve in Fig. 8d). More than 600 events with cross-correlation coefficients higher than 0.95 are identified as FZTW candidates. We further select 33 events (Fig. 9a) that produce high-quality FZTWs (e.g., Fig. 9b) from the candidate events, through template matching of fault-parallel component *S* waveforms at stations B416-B423 (using FZTWs shown in Fig. 7a as the template; Section 3.3.1). These high-quality FZTW candidates show a consistent source-receiver path (top inset of Fig. 9a), indicating the depth of the fault-zone waveguide is likely shallower than 5 km, and there is an optimal range of incidence angle for injecting seismic energy into the fault damage zone beneath array B4 (e.g., Fohrmann et al. 2004).

Compared to FZTW observed from each candidate event (e.g., Fig. 9b), the stacked recordings (Fig. 9c) yield much higher SNRs and can thus provide more reliable and robust estimations of the average fault-zone waveguide properties. Figure 10 presents the inversion results from modeling the stacked waveforms shown in Figure 9c (in red). The best-fitting model yields good waveform fits (Fig. 10a) and suggests a simplified (i.e., vertical rectangular-shaped) fault-zone waveguide with a width of ~280 m, Q value of ~30, and *S*-wave velocity ~80% of the surrounding host rocks (Fig. 10b). The estimated propagation distance inside the waveguide is ~5.4 km (Fig. 10b). Because this includes a propagation component along-strike (i.e., non-vertical incidence angle), it suggests a waveguide depth of ~4 km ($= 5.4/\sqrt{2}$). The estimated average *S*-wave velocity in the host rock is ~4.1 km/s, with the northeast block being ~4.2% faster, consistent with results from the *P*-wave delay time analysis at array B4 (~3% velocity contrast across LVZ#5 with higher velocity in the northeast; Fig. 6g). The parameters of fault-zone models from the last 10 generations (2,000 models) are shown in Figure 10b, along with the corresponding probability density functions computed as the frequency of each parameter value weighted by the fitness values (Ben-Zion et al., 2003). The good waveform fits, combined with the consistency between best fitting parameters and peaks of the probability density functions (Fig. 10b), suggest that the best-fitting model parameters provide robust estimates of the average properties of the fault-zone waveguide.

In addition to FZTWs, we detect in data of stations B420 and B422 (Fig. S13) clear fault-zone head waves (FZHWs) that refract along a bimaterial fault interface (e.g., Ben-Zion, 1990) and arrive ~0.1 s earlier than the direct *P*-wave. The early-arriving FZHWs are inferred from horizontal particle motion analysis modified from the method of Bulut et al. (2012). It is important to note that in the polarization analysis we only focus on the rotation of the horizontal particle motion between FZHW and direct *P*-wave. This is because the polarization direction of horizontal particle motion for the direct *P* wave at stations inside a damage zone (Fig. S13) can deviate significantly from the source-receiver back azimuth. Since the differential time between the FZHW and direct *P*-wave decreases significantly from the northeast (B422) to the southwest (B420) over a short distance (~0.1 km), the observed FZHW is likely traveling along a local interface that is associated with the edge of the damage zone (e.g., Qiu et al., 2017) on the northeast side between stations B422 and B423. Similar FZTW and FZHW signals are also clearly observed in the data of array B2 (e.g., Fig. S14) but not for arrays B1 and B3.

## 4. Discussion

We analyze systematically time delays of *P* arrivals from teleseismic and local earthquakes, *S*-wave amplification, and fault zone trapped waves in data recorded by four long-aperture (4-8 km) arrays at different locations along the rupture zone of the 2019 Mw 7.1 Ridgecrest earthquake (Fig. 2). The analyses allow us to derive information on velocity contrast interfaces and low velocity damage zones at scales of ~100 m associated with the Ridgecrest rupture zone. The results are complementary to tomographic velocity models that provide a regional context but do not resolve the internal structural elements of the Ridgecrest rupture zone imaged in this work.

The delay times of $P$-waves from both teleseismic and local earthquakes, after proper corrections for propagation and topography effects, show clear and consistent velocity contrasts across the rupture zone, with a higher velocity in the northeast at arrays B1 (Figs. 4a and 6a) and B4 (Figs. 4d and 6g). Combining the delay times inferred from teleseismic $P$ waves in Figure 4 and the amplitudes of cross-fault velocity contrast in the left panels of Figure 6, we can estimate the depth extent of the contrast interface beneath each array. For a constant velocity contrast across the fault with an amplitude of $\eta$ extending to a depth of $H_c$, the time delay between teleseismic $P$ arrivals, assuming a vertical angle of incidence, at stations on different sides of the fault is given by

$$\Delta t \approx \eta \cdot H_c / \overline{V_p}, \tag{5}$$

where $\overline{V_p}$ is the average $P$-wave velocity of the upper crust. We set $\overline{V_p} = 5.6$ km/s as inferred from the mean of the average slowness $\bar{s}_j$ (eq. 3) over all event-array pairs. The $H_c$ beneath arrays B1 ($\Delta t = 0.15$ s from Fig. 4a and $\eta = 5.3\%$ from Fig. 6a) and B4 ($\Delta t = 0.25$ s from Fig. 4d and $\eta = 8.8\%$ from Fig. 6g), computed using equation (5), are both ~16 km, suggesting a deep fault interface that likely extends to the seismogenic depth (10-12 km) after taking measurement uncertainties (Figs. 4a and 4d) and non-vertical angle of incidence into account.

We do not estimate the depth $H_c$ for arrays B2 and B3 as the teleseismic $P$-wave delay times $\Delta t$ are highly dependent on the topographic correction (Section 3.1.2; Figs. 4b-c). The cross-fault velocity contrast observed in local $P$-wave delay time patterns resolved at arrays B2 and B3 (Figs. 6c and 6e) suggests a higher velocity in the southwest, the opposite of the polarity obtained at arrays B1 and B4 (Figs. 6a and 6g). Further analysis of the transition zones (Figs. 2b-e) resolved from the modeled cross-fault velocity contrasts (left panels of Fig. 6) indicates that: the observed velocity contrast beneath array B2 is likely an artifact due to insufficient topographic correction; array B3 may detect the velocity contrast across the rupture zone of the Mw 6.4 earthquake; and the broader transition zone beneath array B4 suggests the fault zone at the southeast edge of the Mw 7.1 earthquake rupture is likely not as well localized (e.g., several rupture surface traces; Fig. 2) as those beneath the other three arrays.

Symmetry properties of fault damage zones with respect to the main slip surface can provide information on the direction of earthquake ruptures (e.g., Ben-Zion & Shi, 2005; Dor et al., 2006; Mitchell et al., 2011; Xu et al., 2012). Statistically preferred rupture direction is expected for prominent bimaterial faults (e.g., Ampuero & Ben-Zion, 2008; Andrews and Ben-Zion, 1997; Shlomai & Fineberg, 2016; Weertman, 1980). However, a prominent large-scale velocity contrast is not expected across the Ridgecrest rupture zone based on the regional velocity models (Lee et al., 2014; Shaw et al., 2015; White et al., 2020) and total offset across the structure. The transition zones of the cross-fault velocity contrast resolved at arrays B1 (Fig. 2b) and B3 (Fig. 2d) are asymmetrically distributed to the faster side of the fault surface trace, which is likely indicative of asymmetric rock damage offset to the faster side of the rupture zone for the Mw 7.1 and Mw 6.4 earthquakes, respectively. Since the transition zones resolved at arrays B2 and B4 are not well resolved, we do not discuss results obtained at these two locations (Figs. 2c and 2e).

Good agreement between locations of slower inner cores of the low-velocity zones identified from delay time analyses and the group of stations with amplified *S* waveforms (Fig. 8) is found beneath all four arrays. Combined with the narrow width (300-400 m; right panels of Fig. 6) of the inner cores, these zones that both significantly delay the *P* arrivals and amplify the incoming *S* waveforms are likely representative of localized damage zones, rather than variations in sedimentary thickness that usually yield much wider patterns of *S*-wave amplification. Waveform modeling of FZTWs detected at array B4 yields good waveform fits and an average waveguide with fault-zone parameters comparable to those inferred from previous studies in the SJFZ (Qin et al., 2018; Qiu et al., 2017; Share et al., 2017, 2019): width of ~300 m, Q of ~30, *S*-wave velocity reduction of ~20% inside the damage zone, and depth extent of 3-5 km (Fig. 10).

To further investigate the structures that produce the observed low-velocity zones, we map the inner core and entire span of these zones together with locations of fault surface traces (or their extrapolations) and the surface geology compiled by the USGS in Figure 2. The low-velocity zone (LVZ#1 in Fig. 6b) identified at array B1, in contrast to the resolved transition zone (Fig. 2b), is on the southwest (slower) side of the surface trace of the main rupture zone. There are two well-separated inner cores (Fig. 2b) that yield both large delay times (Fig. 6b) and *S*-wave amplitudes (Fig. 8a). The inner core in the southwest (Fig. 2b) is likely associated with the damage zone of past earthquake ruptures, since it is centered on a surface displacement mapped before the 2019 Ridgecrest earthquake. The northeast inner core (Fig. 2b), however, is likely representative of the damage zone of the Mw 7.1 Ridgecrest earthquake ruptures, as it is centered on the main rupture zone.

At array B2, two low-velocity zones (LVZ #2 and #3) are identified from Figures 6d. Different from the other three arrays, the surface geology beneath array B2 consists of two different types of rocks (alternating playa and igneous rocks; Fig. 2c), which likely explains the weak cross-fault velocity contrast resolved at this location (Figs. 4b and 6c). Both low-velocity zones are centered on the surface traces (or their extrapolations) of the main rupture zone, with the slower inner cores close to the fault traces. Good agreement between locations of low-velocity zones and surface traces of the 2019 Ridgecrest earthquake ruptures is also observed beneath arrays B3 (Fig. 2d) and B4 (Fig. 2e). Since the locations of these low-velocity zones correlate well with the fault surface traces rather than the surface geology, we conclude that: these low-velocity zones with slower inner cores that considerably amplify *S* waveforms depict the fault damage zones of the Mw 7.1 earthquake rupture at arrays B2 and B4, and ruptures of both the Mw 6.4 and Mw 7.1 earthquakes at array B3.

It is interesting to note that we find a clear and coherent secondary phase between *P* and *S* arrivals in waveforms recorded by part of array B4 for more than 10 events located beneath the array. Figure S15b shows such signals for an example event (circle in Fig. S15a). The strong phases are visible at stations B423-B457 (blue curve in Fig. S15b) and correlate well with the shape of the direct *P*-wave but with the opposite first-motion polarity (e.g., Fig. S15d) suggesting the signals are likely reflected or converted waves. Since the array-mean travel time of the direct P-wave is between 1-1.5 s, based on the ~0.5 s differential time between the direct P and the strong secondary waves (e.g., black and blue dashed lines in Fig. S15d), the reflection or conversion interface should be a few kilometers away from the array and is thus likely associated with the Garlock fault in the south rather than the rupture zone of the Mw 7.1 Ridgecrest earthquake (Fig. S15a). Detailed analysis of these candidate reflected/converted phases may require more sophisticated techniques, such as seismic migration of the arrival times and waveform simulation with accurate source information (e.g., focal mechanism) for the understanding of the wave amplitudes. As these secondary signals detected in Figure S15 are outside the scope of this paper, additional analysis of these phases will be the subject of a follow-up study.

## 5. Conclusions

The rupture zone of the Mw 7.1 Ridgecrest earthquake is shown to have seismic velocity contrast interfaces and damage structures with significant along-strike variations of local damage zones. The results are in overall agreement with and complementary to the mapped fault surface traces in the region (e.g., Xu et al., 2020) and previous analyses of aftershocks in the Ridgecrest sequence (e.g., Ross et al., 2019; Cheng & Ben-Zion, 2020).

Delay times of *P* waves from teleseismic and local earthquakes recorded by arrays B1 and B4 resolve velocity contrasts ranging from 5%-9% in Vp across the Ridgecrest rupture zone, which extend to a depth of ~16 km, with the northeast being locally faster. Data recorded by array B3, crossing the surface ruptures of both the Mw 6.4 and Mw 7.1 events, likely detects a ~4% velocity contrast in Vp across the fault that hosted the Mw 6.4 earthquake, with the northwest side having higher velocity. Asymmetric rock damage concentrated on the stiffer side of the fault is seen beneath arrays B1 and B3.

Low-velocity zones that further delay the *P* waves of local seismic events are centered on mapped surface traces of faults associated with both past and the 2019 Ridgecrest earthquake ruptures. Considerable amplification is seen consistently in *S* waveforms recorded at stations within the slower inner core of the identified LVZ. Clear FZTWs are identified at arrays B2 and B4, and inversion of high-quality FZTWs at array B4 indicates a waveguide with average properties comparable to those found in previous studies at sites of the San Jacinto fault zone. Phases identified as FZHWs, associated with the northeast boundary of the fault zone waveguide, are observed at arrays B2 and B4. Coherent candidate reflected or converted waves are observed in data recorded at array B4. Additional analysis of these phases can provide additional constraints on prominent impedance interfaces associated with the Garlock fault and/or the Ridgecrest rupture zone.

## Data Availability

The digital data are available in mseed day volume format, with each component in a separate volume. The data samples are 4 byte floats and consistently sampled at 500 samples/second. Data described in this report are available from the IRIS Data Management Center (https://ds.iris.edu/ds/nodes/dmc/data/). An accompanying report for data acquisition is available from Catchings et al. (2020). Surface traces of the 2019 Ridgecrest earthquake sequence shown in this study were determined by Xu et al. (2020). The geologic data depicted as the background of Figure 2 were obtained from the USGS website (https://mrdata.usgs.gov/geology/state/state.php?state=CA).

## Acknowledgements

The rapid seismic deployment of nodes for the 2019 Ridgecrest earthquake sequence was partially supported by the U.S. Geological Survey, the Southern California Earthquake Center, and the National Science Foundation (grant EAR-1945781). Personnel from the USGS, University of California - Santa Barbara, University of Utah, University of Southern California, and the Naval Air Weapons Station (NAWS) – China Lake, including Elizabeth Berg, Joanne Chan, Coyn Criley, Garet Huddleston, Daniel Langermann Zhenning Ma, Andrew Madsen, Adrian McEvilly, Daniel Mongovin, and Jordan Wang, were invaluable in the rapid response. We thank IRIS-PASSCAL for providing 162 Fairfield Zland 3C nodes and Sandia National Laboratory for providing 54 Fairfield 3C nodes, and the USGS for providing 245 SmartSolo 3C nodes.  We thank Josh Bain, Stephan Bork, Kyle Buck, Darrin Clodt, John Foster, Allen Grossardt, Cyndy Hopkins, Hugh Jones, T.J. Larson, James Lovern, Sean Oleary, Nancy Pahr, Mike Pierce, Jacob Rivera, Vince Wallace, and Shane Williams of the NAWS-China Lake for access and field assistance.  We thank Kate Scharer for coordination assistance with the NAWS. The manuscript benefits from useful comments by two anonymous reviewers, an anonymous Associate Editor and Editor Rachel Abercrombie. The research done in this paper was supported by the National Science Foundation (Award EAR-1945781), the U.S. Department of Energy (Award #DE-SC0016520), and the Southern California

Earthquake Center (based on NSF Cooperative Agreement EAR-1600087 and USGS Cooperative Agreement G17AC00047).

**References**

Aki, K. (1979). Characterization of barriers on an earthquake fault. *Journal of Geophysical Research*. https://doi.org/10.1029/JB084iB11p06140

Allen, R. (1978). Automatic earthquake recognition and timing from signal traces. *Bulletin of the Seismological Society of America*. 68 (5):1521-1532.

Ampuero, J. P., & Ben-Zion, Y. (2008). Cracks, pulses and macroscopic asymmetry of dynamic rupture on a bimaterial interface with velocity-weakening friction. *Geophysical Journal International*, *173*(2), 674–692. https://doi.org/10.1111/j.1365-246X.2008.03736.x

Andrews, D. J., & Ben-Zion, Y. (1997). Wrinkle-like slip pulse on a fault between different materials. *Journal of Geophysical Research B: Solid Earth*. https://doi.org/10.1029/96jb02856

Ben-Zion, Y. (1990). The response of two half spaces to point dislocations at the material interface, *Geophys. J. Int., 101*, 507-528.

Ben-Zion, Y. (1998). Properties of seismic fault zone waves and their utility for imaging low-velocity structures. *Journal of Geophysical Research: Solid Earth*. https://doi.org/10.1029/98jb00768

Ben-Zion, Y., & Aki, K. (1990). Seismic radiation from an SH line source in a laterally heterogeneous planar fault zone. *Bulletin - Seismological Society of America*.

Ben-Zion, Y., & Huang, Y. (2002). Dynamic rupture on an interface between a compliant fault zone layer and a stiffer surrounding solid. *Journal of Geophysical Research*. https://doi.org/10.1029/2001jb000254

Ben-Zion, Y., & Shi, Z. (2005). Dynamic rupture on a material interface with spontaneous generation of plastic strain in the bulk. *Earth and Planetary Science Letters*. https://doi.org/10.1016/j.epsl.2005.03.025

Ben-Zion, Y., Peng, Z., Okaya, D., Seeber, L., Armbruster, J. G., Ozer, N., et al. (2003). A shallow fault-zone structure illuminated by trapped waves in the Karadere-Duzce branch of the North Anatolian Fault, western Turkey. *Geophysical Journal International*. https://doi.org/10.1046/j.1365-246X.2003.01870.x

Brietzke, G. B., & Ben-Zion, Y. (2006). Examining tendencies of in-plane rupture to migrate to material interfaces. *Geophysical Journal International*. https://doi.org/10.1111/j.1365-246X.2006.03137.x

Bulut, F., Ben-Zion, Y., & Bohnhoff, M. (2012). Evidence for a bimaterial interface along the Mudurnu segment of the North Anatolian Fault Zone from polarization analysis of P waves. *Earth and Planetary Science Letters*. https://doi.org/10.1016/j.epsl.2012.02.001

Catchings, R. D., Goldman, M. R., Li, Y. G., & Chan, J. H. (2016). Continuity of the west napa-franklin fault zone inferred from guided waves generated by earthquakes following the 24 august 2014 Mw 6.0 south napa earthquake. *Bulletin of the Seismological Society of America*. https://doi.org/10.1785/0120160154

Catchings, R. D., M.R. Goldman, J.H. Steidl, J.H. Chan, A.A. Allam, C.J. Criley, Z. Ma, D.S. Langermann, G.J. Huddleston, A.T. McEvilly, D.D. Mongovin, E.M. Berg, and Y. Ben-Zion, 2020. Nodal Seismograph Recordings of the 2019 Ridgecrest Earthquake Sequence, *Seism. Res. Lett.*, doi: 10.1785/0220200203.

Chen, K., Avouac, J. P., Aati, S., Milliner, C., Zheng, F., & Shi, C. (2020). Cascading and pulse-like ruptures during the 2019 Ridgecrest earthquakes in the Eastern California Shear Zone. *Nature Communications*, *11*(1), 3–10. https://doi.org/10.1038/s41467-019-13750-w

Cheng, Y. and Y. Ben-Zion, 2020. Variations of earthquake properties before, during and after the 2019 M7.1 Ridgecrest, CA, earthquake, *Geophys*., *Res*., *Lett*., 47, e2020GL089650, doi: 10.1029/2020GL089650.

Cochran, E., Li, Y. G., Shearer, P. M., Barbot, S., Fialko, Y., & Vidale, J. E. (2009). Seismic and geodetic evidence for extensive, long-lived fault damage zones. *Geology*. https://doi.org/10.1130/G25306A.1

Crotwell, H. P., Owens, T. J., & Ritsema, J. (1999). The TauP Toolkit: Flexible Seismic Travel-time and Ray-path Utilities. *Seismological Research Letters*. https://doi.org/10.1785/gssrl.70.2.154

Dahlen, F. A., Hung, S.-H., & Nolet, G. (2000). Frechet kernels for finite-frequency traveltimes - I. Theory. Geophysical Journal International, (141), 157–174. https://doi.org/10.1007/978-3-319-06540-3

Dor, O., Rockwell, T. K., & Ben-Zion, Y. (2006). Geological observations of damage asymmetry in the structure of the San Jacinto, San Andreas and Punchbowl faults in Southern California: A possible indicator for preferred rupture propagation direction. *Pure and Applied Geophysics*. https://doi.org/10.1007/s00024-005-0023-9

Ellsworth, W. L., & Malin, P. E. (2011). Deep rock damage in the san andreas fault revealed by P- and S-type fault-zone-guided waves. *Geological Society Special Publication*. https://doi.org/10.1144/SP359.3

Fohrmann, M., Igel, H., Jahnke, G., & Ben-Zion, Y. (2004). Guided waves from sources outside faults: An indication for shallow fault zone structure? *Pure and Applied Geophysics*. https://doi.org/10.1007/s00024-004-2553-y

Hauksson, E., Yang, W., & Shearer, P. M. (2012). Waveform relocated earthquake catalog for Southern California (1981 to June 2011). *Bulletin of the Seismological Society of America*. https://doi.org/10.1785/0120120010

Huang, Y., Ampuero, J. P., & Helmberger, D. V. (2014). Earthquake ruptures modulated by waves in damaged fault zones. *Journal of Geophysical Research: Solid Earth*. https://doi.org/10.1002/2013JB010724

Igel, H., Ben-Zion, Y., & Leary, P. C. (1997). Simulation of SH- and P-SV-wave propagation in fault zones. *Geophysical Journal International*. https://doi.org/10.1111/j.1365-246X.1997.tb05316.x

Igel, H., Jahnke, G., & Ben-Zion, Y. (2002). Numerical simulation of fault zone guided waves: Accuracy and 3-D effects. *Pure and Applied Geophysics*. https://doi.org/10.1007/s00024-002-8724-9

Jahnke, G., Igel, H., & Ben-Zion, Y. (2002). Three-dimensional calculations of fault-zone-guided waves in various irregular structures. *Geophysical Journal International*. https://doi.org/10.1046/j.1365-246X.2002.01784.x

Jia, Z., Wang, X., & Zhan, Z. (2020). Multifault models of the 2019 Ridgecrest sequence highlight complementary slip and fault junction instability. *Geophysical Research*

*Letters*. https://doi.org/10.1029/2020GL089802

Kennett, B. L. N., & Engdahl, E. R. (1991). Traveltimes for global earthquake location and phase identification. *Geophysical Journal International*. https://doi.org/10.1111/j.1365-246X.1991.tb06724.x

King, G. C. P. (1986). Speculations on the geometry of the initiation and termination processes of earthquake rupture and its relation to morphology and geological structure. *Pure and Applied Geophysics*. https://doi.org/10.1007/BF00877216

Kurzon, I., Vernon, F. L., Ben-Zion, Y., & Atkinson, G. (2014). Ground Motion Prediction Equations in the San Jacinto Fault Zone: Significant Effects of Rupture Directivity and Fault Zone Amplification. *Pure and Applied Geophysics*. https://doi.org/10.1007/s00024-014-0855-2

Lee, E.-J., Chen, P., Jordan, T. H., Maechling, P. B., Denolle, M. A., & Beroza, G. C. (2014). Full-3-D tomography for crustal structure in Southern California based on the scattering-integral and the adjoint-wavefield methods. Journal of Geophysical Research: Solid Earth. https://doi.org/10.1002/2014JB011346

Lewis, M. A., & Ben-Zion, Y. (2010). Diversity of fault zone damage and trapping structures in the Parkfield section of the San Andreas Fault from comprehensive analysis of near fault seismograms. *Geophysical Journal International*. https://doi.org/10.1111/j.1365-246X.2010.04816.x

Lewis, M. A., Peng, Z., Ben-Zion, Y., & Vernon, F. L. (2005). Shallow seismic trapping structure in the San Jacinto fault zone near Anza, California. *Geophysical Journal International*. https://doi.org/10.1111/j.1365-246X.2005.02684.x

Li, Y. G., Leary, P., Aki, K., & Malin, P. (1990). Seismic trapped modes in the Oroville and San Andreas fault zones. *Science*. https://doi.org/10.1126/science.249.4970.763

Li, Y. G., Aki, K., Adams, D., Hasemi, A., & Lee, W. H. K. (1994). Seismic guided waves trapped in the fault zone of the Landers, California, earthquake of 1992. *Journal of Geophysical Research*. https://doi.org/10.1029/94jb00464

Mamada, Y., Kuwahara, Y., Ito, H., & Takenaka, H. (2004). Discontinuity of the Mozumi-Sukenobu fault low-velocity zone, central Japan, inferred from 3-D finite-difference simulation of fault zone waves excited by explosive sources. *Tectonophysics*. https://doi.org/10.1016/j.tecto.2003.09.008

Mitchell, T. M., Ben-Zion, Y., & Shimamoto, T. (2011). Pulverized fault rocks and damage asymmetry along the Arima-Takatsuki Tectonic Line, Japan. *Earth and Planetary Science Letters*. https://doi.org/10.1016/j.epsl.2011.04.023

Mizuno, T., Kuwahara, Y., Ito, H., & Nishigami, K. (2008). Spatial variations in fault-zone structure along the Nojima fault, central Japan, as inferred from borehole observations of fault-zone trapped waves. *Bulletin of the Seismological Society of America*. https://doi.org/10.1785/0120060247

Ozakin, Y., Ben-Zion, Y., Aktar, M., Karabulut, H., & Peng, Z. (2012). Velocity contrast across the 1944 rupture zone of the North Anatolian fault east of Ismetpasa from analysis of teleseismic arrivals. *Geophysical Research Letters*. https://doi.org/10.1029/2012GL051426

Park, S., Tsai, V. C., & Ishii, M. (2019). Frequency-Dependent P Wave Polarization and Its Subwavelength Near-Surface Depth Sensitivity. Geophysical Research Letters. https://doi.org/10.1029/2019GL084892

Peng, Z., Ben-Zion, Y., Michael, A. J., & Zhu, L. (2003). Quantitative analysis of seismic fault zone waves in the rupture zone of the 1992 Landers, California, earthquake: Evidence for a shallow trapping structure. *Geophysical Journal International*. https://doi.org/10.1111/j.1365-246X.2003.02109.x

Qin, L., Ben-Zion, Y., Qiu, H., Share, P. E., Ross, Z. E., & Vernon, F. L. (2018). Internal structure of the san jacinto fault zone in the trifurcation area southeast of anza, california, from data of dense seismic arrays. *Geophysical Journal International*, *213*(1), 98–114. https://doi.org/10.1093/gji/ggx540

Qiu, H., Ben-Zion, Y., Ross, Z. E., Share, P. E., & Vernon, F. L. (2017). Internal structure of the San Jacinto fault zone at Jackass Flat from data recorded by a dense linear array. *Geophysical Journal International*, *209*(3), 1369–1388. https://doi.org/10.1093/gji/ggx096

Ross, Z. E., Idini, B., Jia, Z., Stephenson, O. L., Zhong, M., Wang, X., et al. (2019). Hierarchical interlocked orthogonal faulting in the 2019 Ridgecrest earthquake sequence. Science. https://doi.org/10.1126/science.aaz0109

Rovelli, A., Caserta, A., Marra, F., & Ruggiero, V. (2002). Can seismic waves be trapped inside an inactive fault zone? The case study of Nocera Umbra, Central Italy. *Bulletin of the Seismological Society of America*. https://doi.org/10.1785/0120010288

Share, P. E., Ben-Zion, Y., Ross, Z. E., Qiu, H., & Vernon, F. L. (2017). Internal structure of the San Jacinto fault zone at Blackburn Saddle from seismic data of a linear array. *Geophysical Journal International*, *210*(2), 819–832. https://doi.org/10.1093/gji/ggx191

Share, P. E., Allam, A. A., Ben-Zion, Y., Lin, F.-C., & Vernon, F. L. (2019). Structural Properties of the San Jacinto Fault Zone at Blackburn Saddle from Seismic Data of a Dense Linear Array. *Pure and Applied Geophysics*, *176*(3), 1169–1191. https://doi.org/10.1007/s00024-018-1988-5

Shaw, J. H., Plesch, A., Tape, C., Suess, M. P., Jordan, T. H., Ely, G., et al. (2015). Unified Structural Representation of the southern California crust and upper mantle. Earth and Planetary Science Letters. https://doi.org/10.1016/j.epsl.2015.01.016

Shlomai, H., & Fineberg, J. (2016). The structure of slip-pulses and supershear ruptures driving slip in bimaterial friction. *Nature Communications*. https://doi.org/10.1038/ncomms11787

Spudich, P., & Olsen, K. B. (2001). Fault zone amplified waves as a possible seismic hazard along the Calaveras fault in central California. *Geophysical Research Letters*. https://doi.org/10.1029/2000GL011902

Thakur, P., Huang, Y., & Kaneko, Y. (2020). Effects of Low-Velocity Fault Damage Zones on Long-Term Earthquake Behaviors on Mature Strike-Slip Faults. *Journal of Geophysical Research: Solid Earth*. https://doi.org/10.1029/2020JB019587

Vidale, J., Helmberger, D. V., & Clayton, R. W. (1985). Finite-difference seismograms for SH waves. *Bulletin of the Seismological Society of America*.

Wang, Y., Allam, A. A., & Lin, F.-C. (2019). Imaging the Fault Damage Zone of the San Jacinto Fault Near Anza With Ambient Noise Tomography Using a Dense Nodal Array. *Geophysical Research Letters*. https://doi.org/10.1029/2019GL084835

Weertman, J. (1980). Unstable slippage across a fault that separates elastic media of different elastic constants. *Journal of Geophysical Research*, *85*(B3), 1455–1461. https://doi.org/10.1029/JB085iB03p01455

White, M. C., Fang, H., Catchings, R. D., Goldman, M. R., Steidl, J. H., & Ben-Zion, Y. (2020, 07). Detailed traveltime tomography and seismicity around the 2019 M7.1 Ridgecrest, CA, earthquake using dense rapid-response seismic data. Poster Presentation at 2020 SCEC Annual Meeting.

Xu, S., Ben-Zion, Y., & Ampuero, J. P. (2012). Properties of inelastic yielding zones generated by in-plane dynamic ruptures-II. Detailed parameter-space study. *Geophysical Journal International*. https://doi.org/10.1111/j.1365-246X.2012.05685.x

Xu, X., Sandwell, D. T., & Smith-Konter, B. (2020). Coseismic displacements and surface fractures from sentinel-1 InSAR: 2019 Ridgecrest earthquakes. *Seismological Research Letters*, *91*(4), 1979–1985. https://doi.org/10.1785/0220190275

Zhu, L., & Kanamori, H. (2000). Moho depth variation in southern California from teleseismic receiver functions. *Journal of Geophysical Research: Solid Earth*, *105*(B2), 2969–2980. https://doi.org/10.1029/1999JB900322

Figure 1. Location map for the 2019 Ridgecrest earthquake sequence (colored circles, square, and stars) and four linear arrays (B1, B2, B3, and B4 as red, green, blue, and purple triangles, respectively) analyzed in this study. The catalog of Hauksson et al. (2012, extended to 2019) is used for earthquake locations, with color representing the focal depth (colorbar). Epicenters of the 2019 Mw 6.4 and Mw 7.1 Ridgecrest earthquakes are marked as stars. Bandpass filtered waveforms, fault zone head waves, and fault zone trapped waves of an example event (orange square) recorded at array B4 are shown in Figs. S12, S13a, and 7a. Fault surface traces are depicted as black lines with ruptures of the 2019 Ridgecrest earthquake sequence being thicker. Near-fault seismic events outlined by the red box are analyzed in sections 3.2 and 3.3. The background gray colors indicate the local topography. WLSZ – Walker Lane Shear Zone; ECSZ – Eastern California Shear Zone; EF – Elsinore Fault; GF – Garlock Fault; SAF – San Andreas Fault; SJF – San Jacinto Fault.

Figure 2. Zoomed-in maps of all the Ridgecrest linear arrays (triangles) in (a) and B1-B4 in (b)-(e), respectively. Color of the map background depicts the surface geology (i.e., rock types; legend in (a)) extracted from the USGS website (see Data Availability). The station elevation is illustrated by the color of the triangles in (b)-(e). The green circle and black lines denote the center of the array and surface traces of faults associated with the 2019 Mw 7.1 and Mw 6.4 Ridgecrest earthquakes (red and blue stars), respectively. The green bars outline the span of the low-velocity zones identified in the local *P*-wave delay time analysis (Section 3.2), whereas the red bars illustrate the region of the slower inner cores (Fig. 6). The blue arrows depict the extent of the transition zone pointing from the slower to faster crustal blocks (black solid curves in Fig. 6).

Figure 3. (a) Locations of array B4 (triangle) and four teleseismic events analyzed in this study (stars), with the red star indicating the event analyzed in (b)-(c). (b) *P* waves recorded on vertical-component sensors of array B4 for the target teleseismic event are illustrated in colors with red and blue indicating positive and negative values. The *P*-wave arrival time predicted from the model IASP91 is used to align the

*P* waveforms and is set to be zero in the time axis. The *P* waveforms are bandpass filtered twice. After applying a bandpass filter between 0.5 Hz and 2 Hz, the array-mean envelope function and an array-mean *P*-wave pick are computed and depicted as the curve and the vertical solid line in black, respectively. (c) Amplitude spectrum averaged over the entire array with the red star and horizontal dashed lines indicating the peak frequency and median of the amplitude spectrum between 0.5 Hz and 2 Hz, respectively. Then, a second bandpass filter between the frequency range outlined by the vertical dashed lines in (c) is applied. The red dashed curve in (b) depicts the teleseismic *P*-wave delay times, measured using the *P* waveforms tapered between the vertical dashed lines (± one dominant period relative to the array-mean *P*-wave pick).

Figure 4. Teleseismic *P*-wave delay times for arrays (a) B1, (b) B2, (c) B3, and (d) B4. The colored stars indicate *P*-wave delay times measured from different teleseismic events and are labeled in the legend by the corresponding peak frequency of the array-mean *P*-wave amplitude spectrum. The black dots depict the delay-time pattern averaged over all teleseismic events, with error bars representing the standard deviation of the mean. The blue and red dashed curves illustrate the delay times after a topographic correction, assuming constant *P*-wave velocities of 2 km/s and 4 km/s. The green bars outline the span of the low-velocity zones identified in local *P*-wave delay time analysis (Section 3.2), while the red bars illustrate the region of the slower inner cores (Fig. 6).

Figure 5. (a) *P* waveforms of an example local seismic event, shown as the blue star in (c), recorded on vertical-component sensors of array B1. Waveform at each station is normalized by its corresponding maximum amplitude and bandpass filtered between 0.5 Hz and 20 Hz. Red stars denote the automatic *P* picks. (b) Same as (a) but shown in slowness domain, i.e., the time axis of each station is divided by the corresponding hypocentral distance. (c) Distribution of seismic events that pass the selection criteria (Section 3.2.1) for array B1 (red triangles) are shown as circles with color representing the focal depth. Events used in the delay time analysis (Section 3.2) for array B1 are outlined by the red box (Area1) and the results are shown in

Figs. 6a-b. Data from events outside the red box (Area2 and Area3) are also analyzed (Figs. S8c-d). The black lines represent fault surface traces. Earthquakes that are excluded from the delay-time analysis at array B1 are shown as grey dots.

Figure 6. Statistical analysis of local *P*-wave arrival patterns for all four arrays. (a) Red dots illustrate the *P*-wave relative slowness variation within array B1, averaged over 189 local seismic events with depth > 5 km and along-fault distance < 5 km relative to the array. The error bars represent a range of three standard deviations of the mean about each respective mean value. The solid black lines depict the contribution associated with a *P*-wave velocity contrast (~5.3% faster in the NE) across the fault beneath the array. The corresponding mean *P*-wave delay time variation is illustrated as the blue curve with dashed blue curves indicating the uncertainties. (b) The *P*-wave delay time variation after removing the modeled cross-fault velocity contrast (the solid black curve in (a)) is shown in blue for array B1. The green dashed vertical lines outline the identified low velocity zone (LVZ), where *P* waves are significantly delayed with respect to the background level (black dashed line). The red dashed vertical lines denote the inner core of the LVZ, i.e., the amplitude of the blue curve is large whereas its gradient is relatively small. The gray-scale heat map of values for relative slowness and delay times after the cross-fault-velocity-contrast correction obtained at each station for all analyzed events is illustrated in (a) and (b), respectively. PDF – Probability Density Function. Results for arrays B2, B3, and B4 are shown in (c)-(d), (e)-(f), and (g)-(h), respectively.

Figure 7. (a) Fault zone trapped waves (FZTWs) following the *S*-wave arrivals for an example event (square in Fig. 1) observed at the fault-parallel component of array B4. The waveforms are preprocessed following the steps of Figure S6 of Qiu et al. (2017). The blue bar outlines the stations with FZTWs. (b) Red dots and blue stars denote the distributions of normalized peak ground velocities (PGV) and root mean square amplitudes (RMS) of the *S* waveforms shown in (a). The black curve represents the likelihood of FZTW, i.e., the normalized multiplication of PGV and RMS values, and is used to identify FZTW candidates.

Figure 8. *S*-wave amplification analysis for arrays B1-B4 in (a)-(d). Gray-scale heat maps of FZTW-likelihood values (e.g., black curve in Fig. 7b) computed at each station in the array for all analyzed events are shown. Red dots depict the likelihood curve averaged over all analyzed events. Error bars represent a range of two standard deviations of the mean about each respective mean value. The bottom green bar marks the low velocity zone (LVZ) identified from the local *P*-wave delay time analysis (green dashed lines in Fig. 6), whereas the red bar illustrates the slower inner core of the LVZ (red dashed lines in Fig. 6). The blue bar in (d) outlines the stations with FZTWs at array B4 (blue bar in Fig. 7a).

Figure 9. (a) Locations of earthquakes (gray dots) analyzed in section 3.3. FZTW candidates identified through template matching, with correlation coefficient greater than 0.85 marked as stars and color representing the focal depth. Red triangles denote the location of array B4. The along-fault cross section of seismicity (dots and stars) and array B4 (triangle) are shown in the top inset. (b) FZTWs recorded at stations B416-B423 for nine high-quality candidate events (red) with the highest correlation coefficients. The template waveforms (Fig. 7a) are shown in black. The array-mean *S* pick and correlation coefficient of each candidate event are labeled in the top left. (c) Comparison between FZTWs of the reference event (in black) and those averaged over all the high-quality candidate events (in red) observed between stations B416-B423.

Figure 10. Inversion results for FZTWs observed between stations B416-423, averaged over candidates shown in Figure 9a. (a) Comparison between synthetic waveforms (red) computed using the best-fitting model parameters (black dots in (b)) and the observed FZTWs (in black). (b) Fitness values of fault-zone model parameters from the last 10 generations of the inversion (green dots). The best-fitting parameters (black circles) are displayed in each panel and used to generate the synthetic waveforms shown in (a). Black curve indicates the probability density function of model parameters shown as green dots.

**Figure 1.**

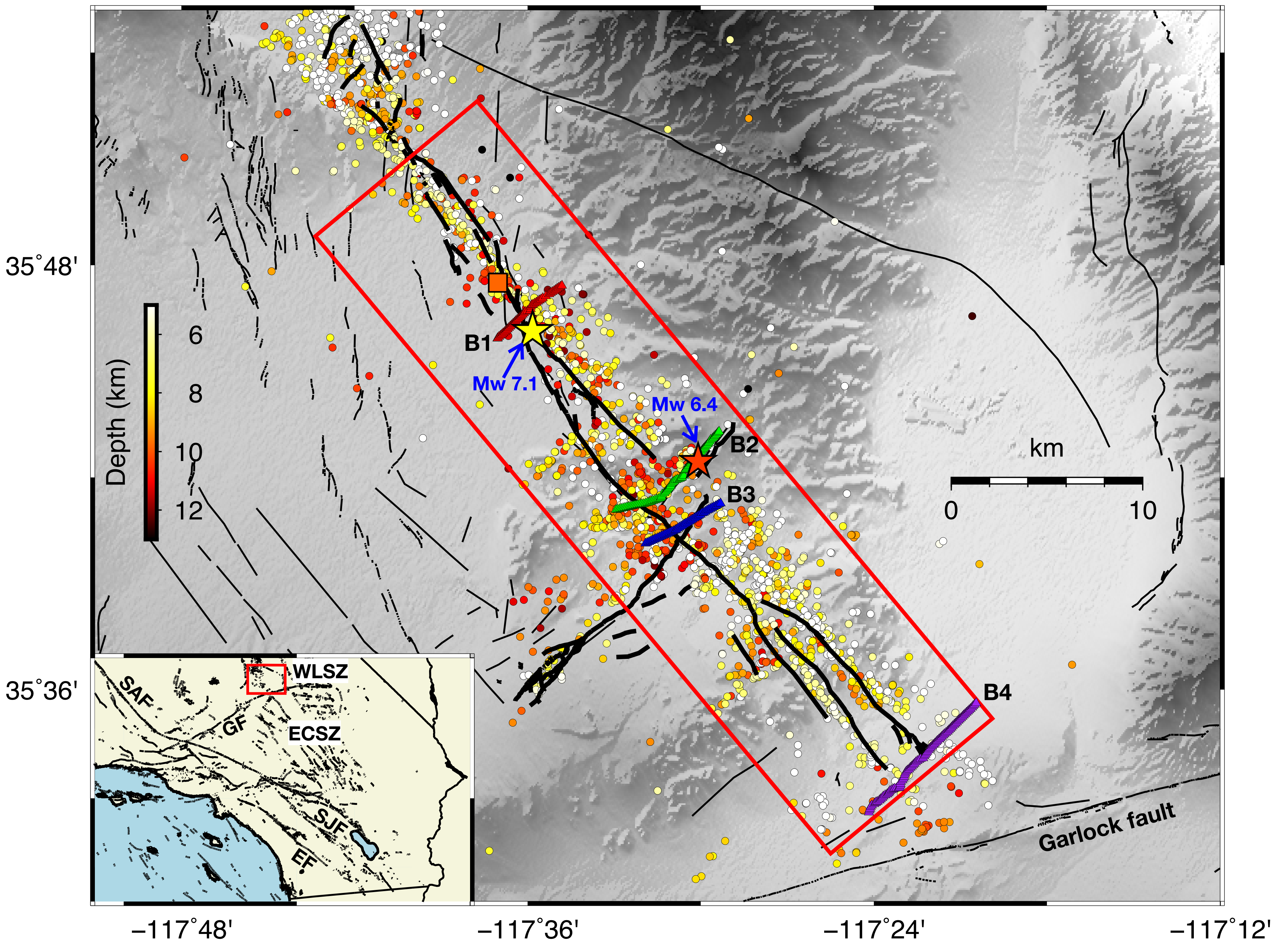

35°48'
35°36'
−117°48'
−117°36'
−117°24'
−117°12'
Depth (km)
6
8
10
12
B1
Mw 7.1
Mw 6.4
B2
B3
B4
km
0
10
Garlock fault
WLSZ
SAF
GF
ECSZ
SJF
EF

**Figure 2.**

Predominant rock type
Granodiorite
Schist
Water
Sandstone
Conglomerate
Alluvium
LVZ
Inner core
Mw 7.1
Mw 6.4
B1
B2
B3
B4
(a)
(b)
(c)
(d)
(e)
Slow
Fast
1 km
Topography (km)
Garlock fault

**Figure 3.**

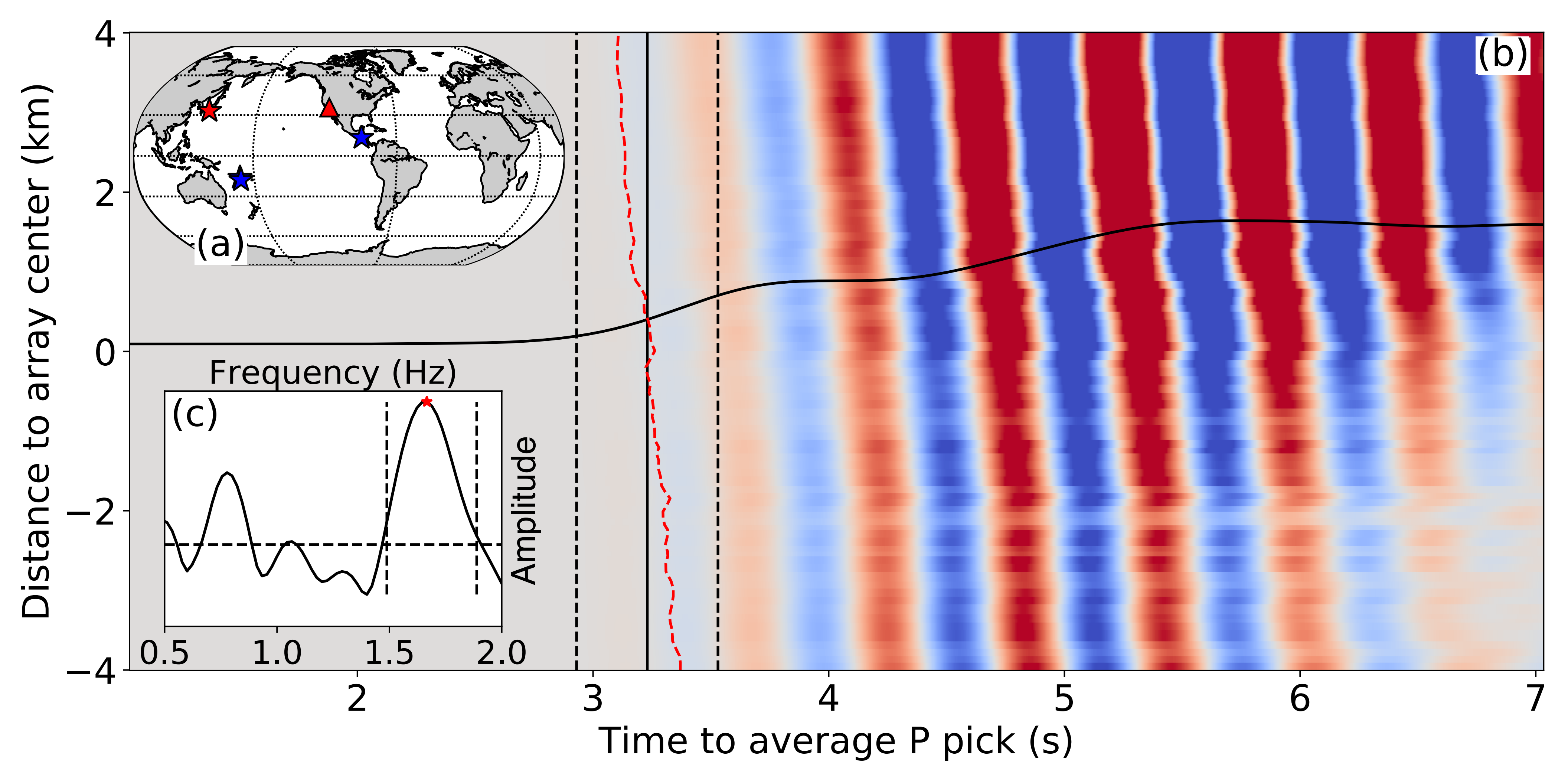

(a)
(b)
(c)
Distance to array center (km)
Time to average P pick (s)
Frequency (Hz)
Amplitude
4
2
0
−2
−4
2
3
4
5
6
7
0.5
1.0
1.5
2.0

**Figure 4.**

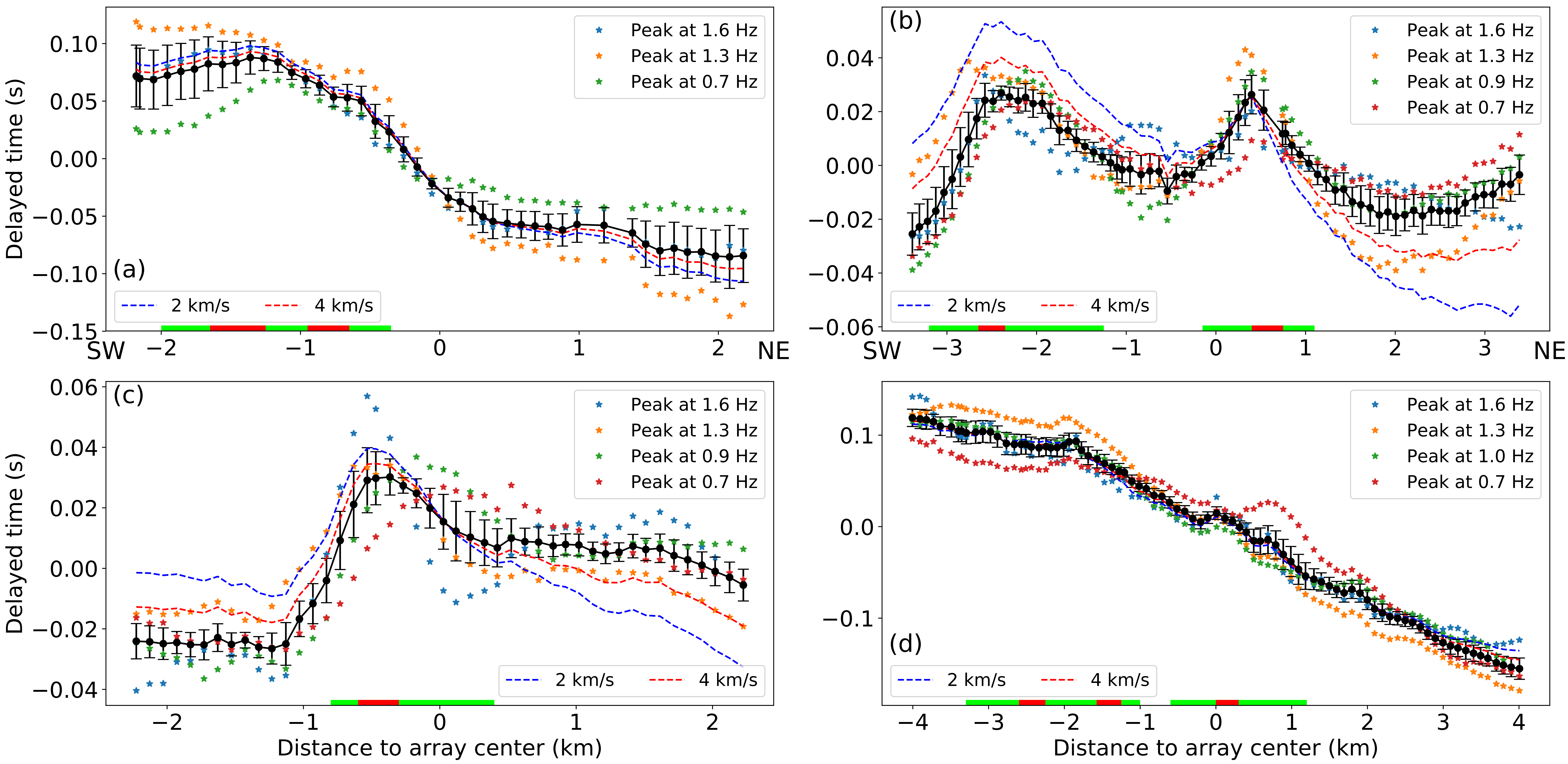
(a)
(b)
(c)
(d)
Peak at 1.6 Hz
Peak at 1.3 Hz
Peak at 1.0 Hz
Peak at 0.9 Hz
Peak at 0.7 Hz
2 km/s
4 km/s
Delayed time (s)
Distance to array center (km)
SW
NE

**Figure 5.**

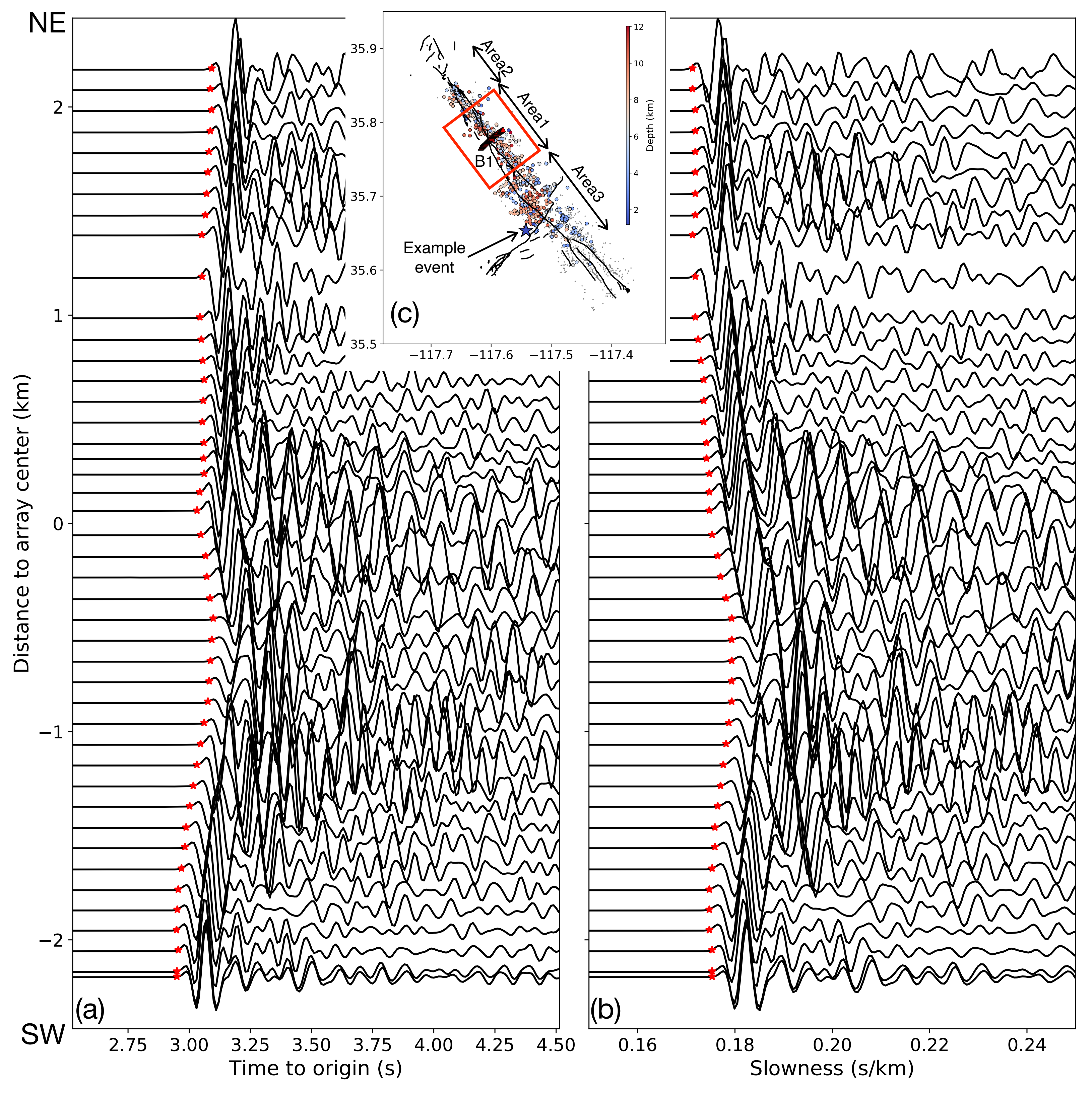

NE
SW
Distance to array center (km)
2
1
0
−1
−2
(a)
2.75
3.00
3.25
3.50
3.75
4.00
4.25
4.50
Time to origin (s)
(b)
0.16
0.18
0.20
0.22
0.24
Slowness (s/km)
(c)
35.9
35.8
35.7
35.6
35.5
−117.7
−117.6
−117.5
−117.4
Area2
Area1
Area3
B1
Example
event
Depth (km)
12
10
8
6
4
2

**Figure 6.**

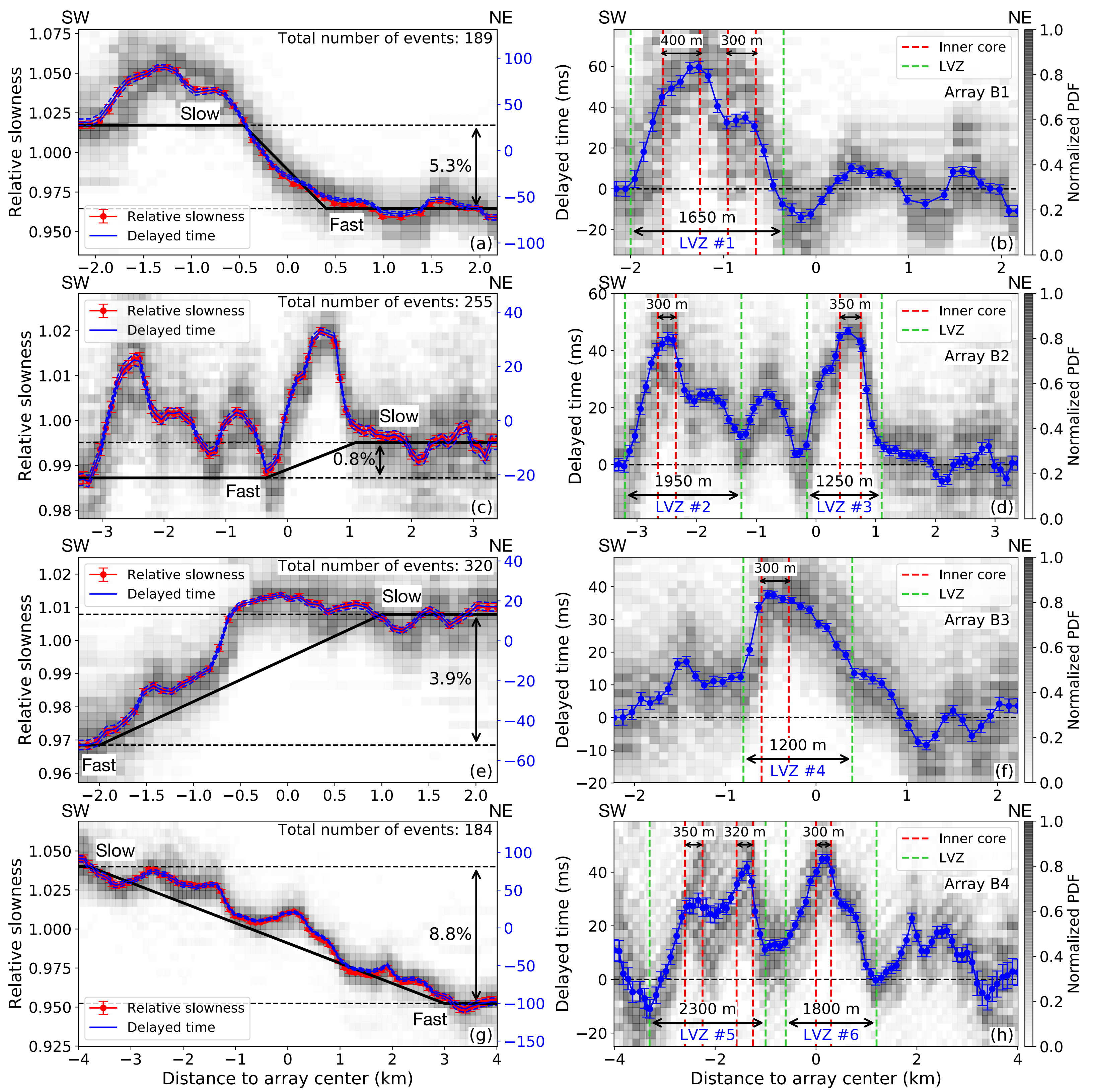

SW
NE
Total number of events: 189
Relative slowness
Slow
Fast
5.3%
Relative slowness
Delayed time
(a)
400 m
300 m
Inner core
LVZ
Array B1
Delayed time (ms)
1650 m
LVZ #1
(b)
Normalized PDF
Total number of events: 255
Slow
Fast
0.8%
(c)
300 m
350 m
Array B2
1950 m
1250 m
LVZ #2
LVZ #3
(d)
Total number of events: 320
3.9%
(e)
Array B3
1200 m
LVZ #4
(f)
Total number of events: 184
8.8%
(g)
350 m
320 m
300 m
Array B4
2300 m
1800 m
LVZ #5
LVZ #6
(h)
Distance to array center (km)

**Figure 7.**

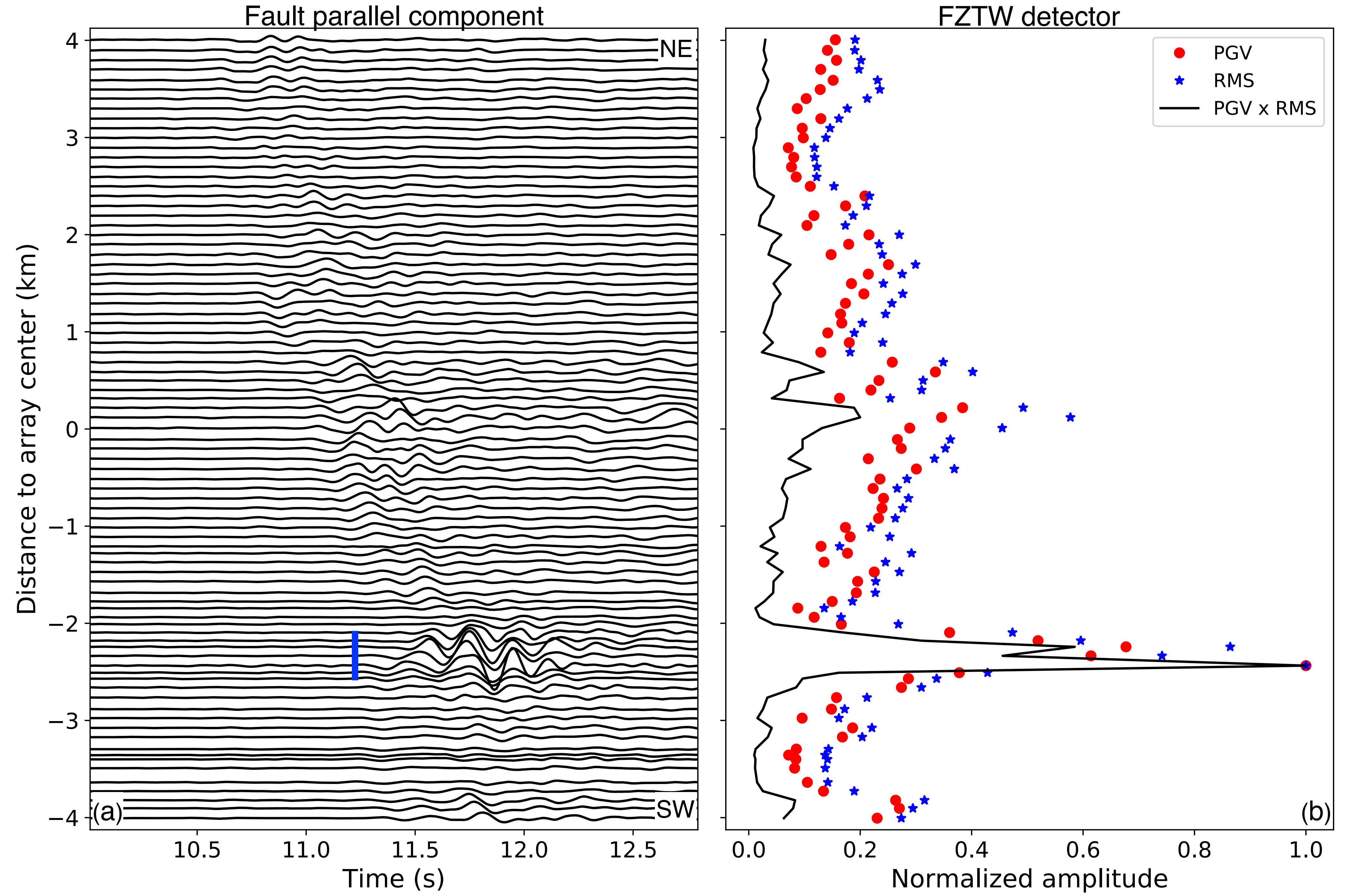

Fault parallel component
FZTW detector
NE
SW
(a)
(b)
Distance to array center (km)
Time (s)
Normalized amplitude
PGV
RMS
PGV x RMS
4
3
2
1
0
−1
−2
−3
−4
10.5
11.0
11.5
12.0
12.5
0.0
0.2
0.4
0.6
0.8
1.0

**Figure 8.**

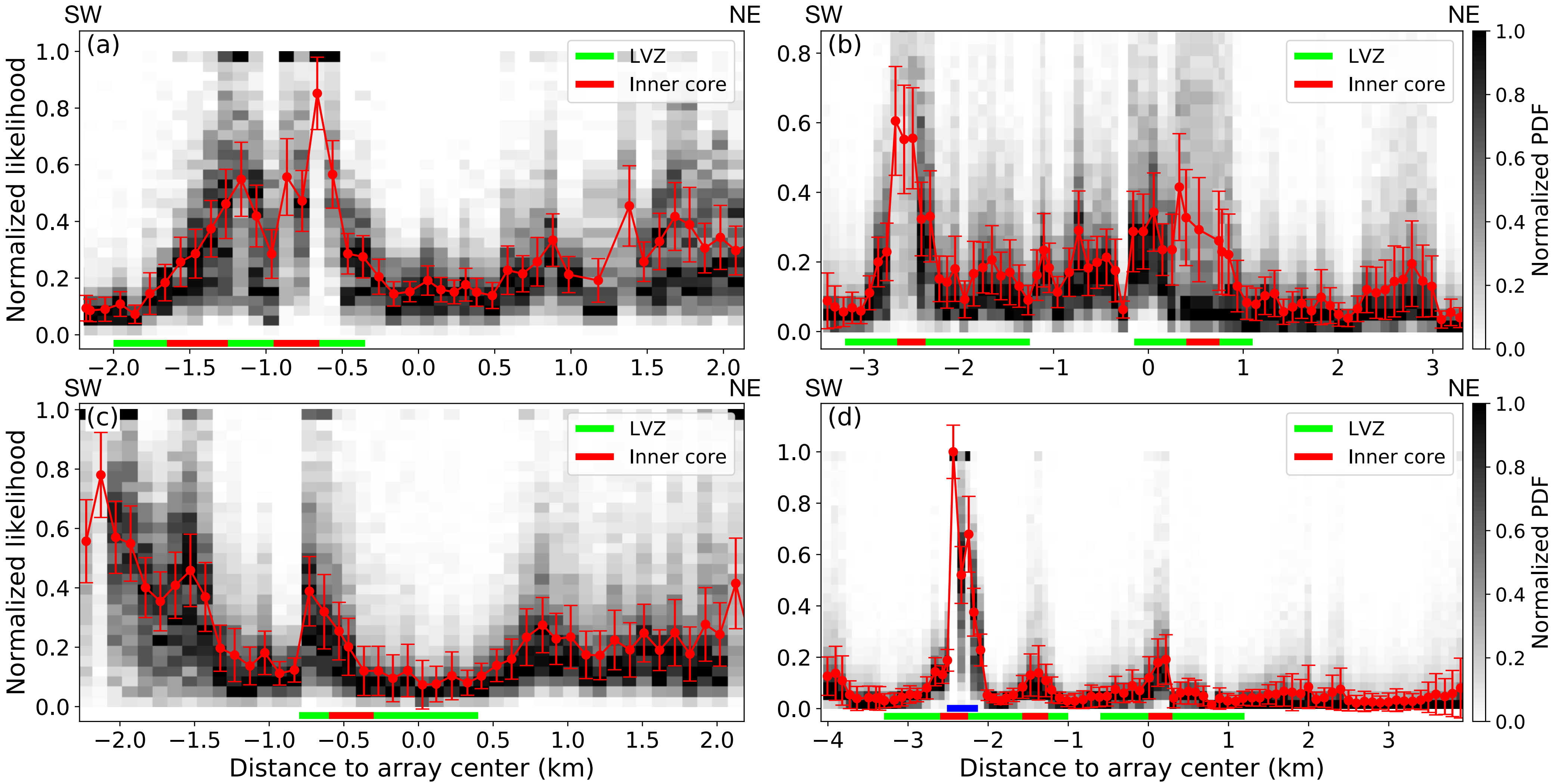
SW
NE
(a)
(b)
(c)
(d)
LVZ
Inner core
Normalized likelihood
Normalized PDF
Distance to array center (km)

**Figure 9.**

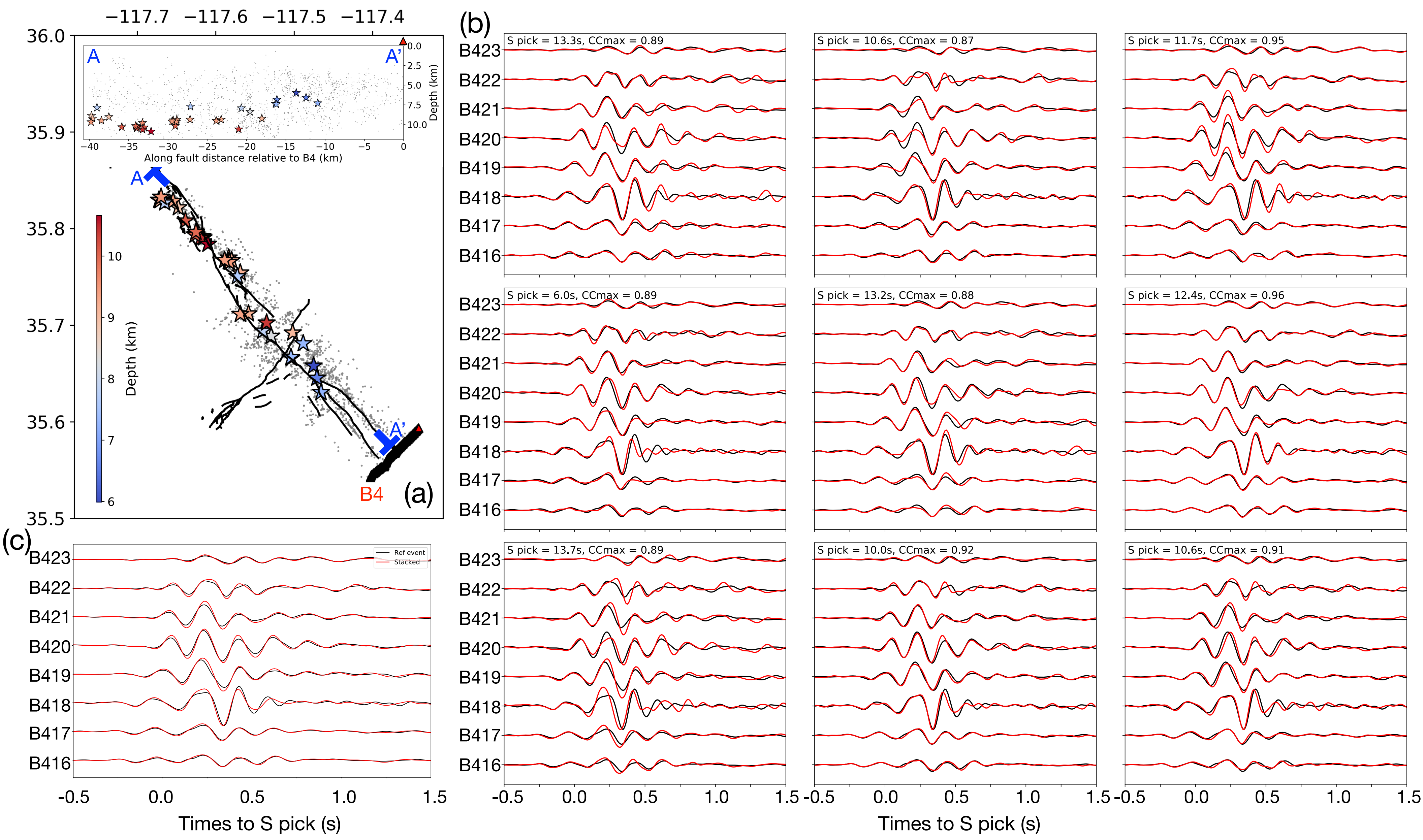

(a)
(b)
(c)
−117.7
−117.6
−117.5
−117.4
36.0
35.9
35.8
35.7
35.6
35.5
A
A'
B4
Depth (km)
Along fault distance relative to B4 (km)
S pick = 13.3s, CCmax = 0.89
S pick = 10.6s, CCmax = 0.87
S pick = 11.7s, CCmax = 0.95
S pick = 6.0s, CCmax = 0.89
S pick = 13.2s, CCmax = 0.88
S pick = 12.4s, CCmax = 0.96
S pick = 13.7s, CCmax = 0.89
S pick = 10.0s, CCmax = 0.92
S pick = 10.6s, CCmax = 0.91
B423
B422
B421
B420
B419
B418
B417
B416
Ref event
Stacked
Times to S pick (s)

**Figure 10.**

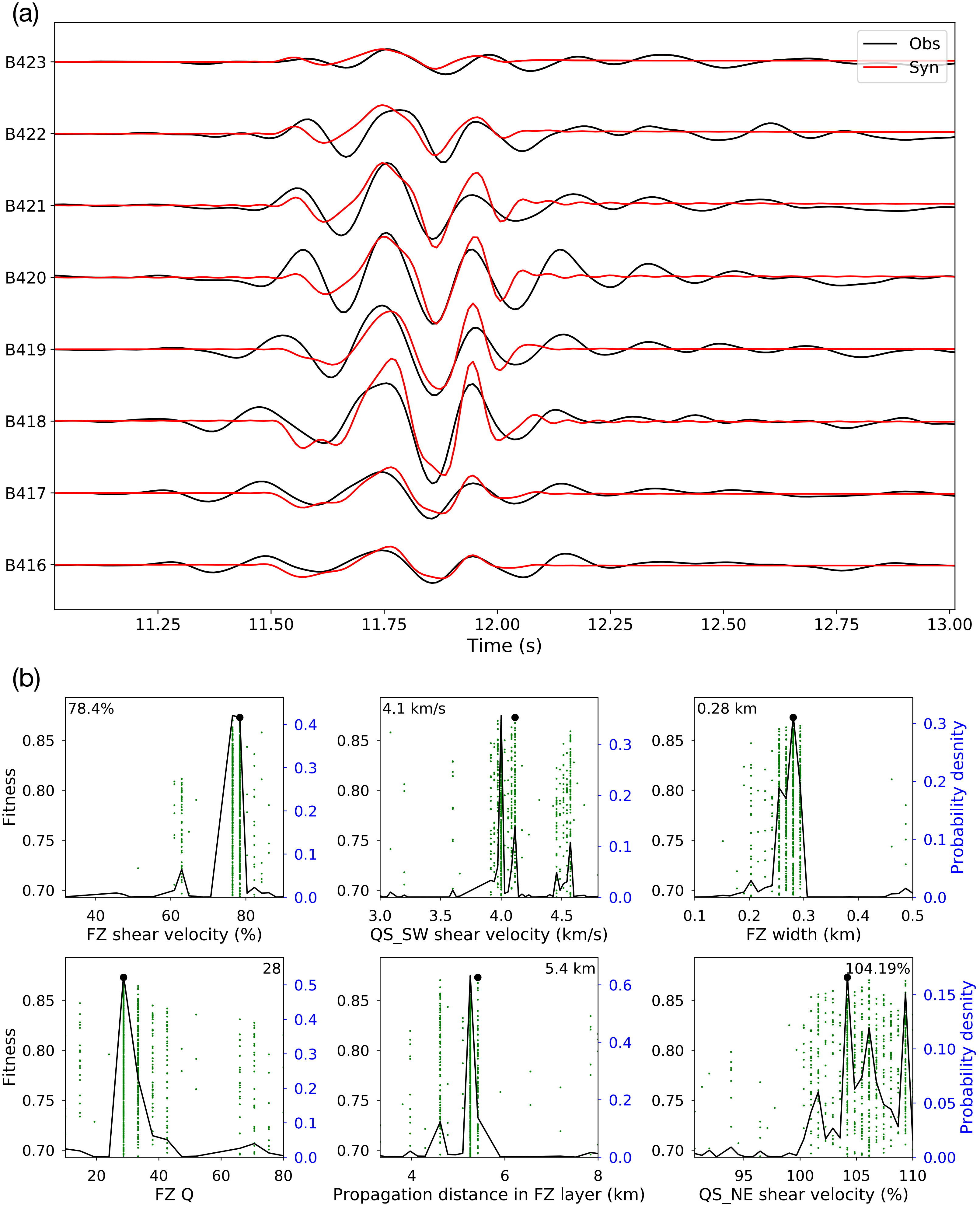

(a)
B423
B422
B421
B420
B419
B418
B417
B416
Obs
Syn
11.25
11.50
11.75
12.00
12.25
12.50
12.75
13.00
Time (s)
(b)
78.4%
Fitness
FZ shear velocity (%)
4.1 km/s
QS_SW shear velocity (km/s)
0.28 km
FZ width (km)
Probability desnity
28
FZ Q
5.4 km
Propagation distance in FZ layer (km)
104.19%
QS_NE shear velocity (%)